



Jones, T. J., McNamara, K., Eychenne, J., Rust, A. C., Cashman, K. V., Scheu, B., & Edwards, R. (2016). Primary and secondary fragmentation of crystal-bearing intermediate magma. *Journal of Volcanology and Geothermal Research*, 327, 70-83.  
<https://doi.org/10.1016/j.jvolgeores.2016.06.022>

Peer reviewed version

License (if available):  
CC BY-NC-ND

Link to published version (if available):  
[10.1016/j.jvolgeores.2016.06.022](https://doi.org/10.1016/j.jvolgeores.2016.06.022)

[Link to publication record in Explore Bristol Research](#)  
PDF-document

This is the accepted author manuscript (AAM). The final published version (version of record) is available online via Elsevier at <http://dx.doi.org/10.1016/j.jvolgeores.2016.06.022>. Please refer to any applicable terms of use of the publisher.

## **University of Bristol - Explore Bristol Research**

### **General rights**

This document is made available in accordance with publisher policies. Please cite only the published version using the reference above. Full terms of use are available:  
<http://www.bristol.ac.uk/pure/about/ebr-terms>

Manuscript Number: VOLGEO5083R1

Title: Primary and secondary fragmentation of crystal-bearing  
intermediate magma

Article Type: Research paper

Keywords: Volcanic ash; Fragmentation; Broken crystals; Milling;  
Fractals; X-ray computed tomography

Corresponding Author: Mr. Thomas James Jones,

Corresponding Author's Institution: Durham University

First Author: Thomas James Jones

Order of Authors: Thomas James Jones; Keri McNamara; Julia Eychenne;  
Alison C Rust; Katharine V Cashman; Bettina Scheu; Robyn Edwards

Abstract: Crystal-rich intermediate magmas are subjected to both primary and secondary fragmentation processes, each of which may produce texturally distinct tephra. Of particular interest for volcanic hazards is the extent to which each process contributes ash to volcanic plumes. One way to address this question is by fragmenting pyroclasts under controlled conditions. We fragmented pumice samples from Soufriere Hills Volcano (SHV), Montserrat, by three methods: rapid decompression in a shock tube-like apparatus, impact by a falling piston, and milling in a ball mill. Grain size distributions of the products reveal that all three mechanisms produce fractal breakage patterns, and that the fractal dimension increases from a minimum of  $\sim 2.1$  for decompression fragmentation (primary fragmentation) to a maximum of  $\sim 2.7$  by repeated impact (secondary fragmentation). To assess the details of the fragmentation process, we quantified the shape, texture and components of constituent ash particles. Ash shape analysis shows that the axial ratio increases during milling and that particle convexity increases with repeated impacts. We also quantify the extent to which the matrix is separated from the crystals, which shows that secondary processes efficiently remove adhering matrix from crystals, particularly during milling (abrasion). Furthermore, measurements of crystal size distributions before (using x-ray computed tomography) and after (by componentry of individual grain size classes) decompression-driven fragmentation show not only that crystals influence particular size fractions across the total grain size distribution, but also that free crystals are smaller in the fragmented material than in the original pumice clast. Taken together, our results confirm previous work showing both the control of initial texture on the primary fragmentation process and the contributions of secondary processes to ash formation. Critically, however, our extension of previous analyses to characterization of shape, texture and componentry provides new analytical tools that can be used to assess contributions of secondary processes to ash deposits of uncertain or mixed origin. We illustrate this application with examples from SHV deposits.



Prof Jurgen W Neuberg  
Editor: JVGR

June 28, 2016

**Re: Revised JVGR Manuscript VOLGEO5083R1**

Dear Prof Jurgen Neuberg,

We are pleased that you have elected to accept our manuscript "*Primary and secondary fragmentation of crystal-bearing intermediate magma*", pending minor revisions, for publication in JVGR. In our attached revision we have addressed all of the suggestions of the referee. All our responses to the particular suggestions can be found in our point-by-point reply.

Thank you for handling this manuscript so efficiently.

Yours truly,

Thomas Jones

Corresponding Author Contact Details:

Thomas Jones  
Department of Earth Sciences  
Durham University  
South Road, Durham, UK, DH1 3LE  
[t.j.jones@durham.ac.uk](mailto:t.j.jones@durham.ac.uk)

### **Point-by-point redress of reviewer comments**

**JVGR submission:** Primary and secondary fragmentation of crystal bearing intermediate magma

**Manuscript number:** VOLGEO5083

**Authors:** Thomas J. Jones, Keri McNamara, Julia Eychenne, Alison C. Rust, Katharine V. Cashman, Bettina Scheu and Robyn Edwards

Reviewer comments are shown in standard font, responses and respective changes are shown in *red italic font*

**Reviewer #1:** In this article, the authors used original experimental data to better understand the control of crystals on fragmentation of magma. The paper is very clear and well written and the conclusions are convincing. This field of research is active and many papers have been published in this subject, but the present contribution adds something new to the literature (the detailed analysis of the control of crystals). I thus support its publication in the journal of volcanological and geothermal research. I have only two major points and a couple of minor points the authors may wish to take into account in the final version of the manuscript.

#### **Main points:**

(i) In a recent paper, Costa et al. "Assessing tephra total grain-size distribution: Insights from field data analysis", Earth and Planetary Science Letters 443 (2016) 90-107, suggest that the Total Grain Size Distribution of volcanic deposits is better describe by (at least) two subpopulations, a coarse and a fine one, with two different power law exponents. It is my understanding that the present paper deals with the fine population rather than with the coarse one. This may explain the different between the authors' conclusion on the evolution of  $D$  (that here remains lower than 3) and the one of Kaminski and Jaupart 1998 (where  $D$  becomes larger than 3). It is possible that the effect of crystals is more important on the fine fraction than on the coarse one? Some figures may indicate a larger decrease of the number of the largest fragments in the distribution than predicted by the best fit  $D$  exponent. I suggest the authors add a few words on that question in the discussion.

*Thank you for highlighting this recent work. In direct response to your question you can see the grain size fractions included in the power-law fit in Figure S1. Where possible we deal with the total grain size distribution collected from the experiments not just a coarse or fine fraction. A maximum of two data points were excluded at either the coarse or fine tail of our experimental data set. We therefore cannot produce multiple fractal dimensions; it would be unreasonable to fit a line between one or two data points. We have added the following sentences to clarify our analysis approach. "In some cases one or two data points are excluded at the coarse or fine tail. The open circles in Figure S1 represent these data points."*

*Lastly, in response to: "It is my understanding that the present paper deals with the fine population rather than with the coarse one. This may explain the different between the authors' conclusion on the evolution of  $D$  (that here remains lower than*

*3) and the one of Kaminski and Jaupart 1998 (where D becomes larger than 3).” For fractal dimensions (D values) > 3 it is the small grain size fraction that controls the power law. So dealing with the fine fraction cannot be the reason we see a small D value. Only studying the fine grain size fractions should actually act to raise D.*

(ii) The application of the model to the SHC deposits is interesting. However it does not allow one to fully entangle the relative contribution of the different parameters that impact the final grain size distribution because the starting material is not exactly the same. I wonder if the analysis can be carried on on samples coming from fall and flow deposits produced by the same eruption, such as MSH 1980. This should help to emphasize the role of secondary fragmentation in the GSD of PDC.

*We selected the two SHV events based on their eruption characteristics. The March 1997 event produced a tephra deposit that was entirely formed of co-PDC ash (therefore solely produced by secondary fragmentation). Whereas the September 1997 tephra contains contributions from both vent-derived and co-PDC ash. It should have products from both primary and secondary fragmentation. Using these two events with different eruption characteristics we can investigate the influence of abrasion in PDCs.*

*These natural data are included as an example of how one could use our analysis on naturally fragmented material. SHV eruptive material was also chosen because we used SHV pumice as the starting material in all our experiments. We have expanded the first paragraph of Section 5.4 to make this rationale clearer. Unfortunately conducting analysis on MSH material would be beyond the scope of this study. Hopefully using the framework which we set out for classifying and identifying primary and secondary fragmentation products future work will investigate tephra deposits like those at MSH.*

#### Minor points:

- The third highlight seems to miss the main verb.

*The third highlight is now changed to “We define a milling index (Adherence Factor) that quantifies the degree of abrasion”*

- line 61: secondary fragmentation can also occur in the conduit (through collisions)

*We have now made this sentence clearer to include subsurface processes. The new sentence reads: “Volcanic ash can form by both primary and secondary processes; the former from volatile driven decompression during magmatic ascent and the latter from processes after the fragmentation front such as pyroclastic density currents (PDCs) and collisions within the conduit.”*

- Figure 3: the effect of temperature is the most notable. But I think it is not really discussed in the paper (or I have missed it). Do you have some explanation for the control of temperature on GSD?

*We have chosen to simply describe this effect (line 300). We have ideas why temperature induced grain size coarsening occurs, however on a singular pair of results we did not feel there was sufficient evidence to speculate on the cause of this difference.*

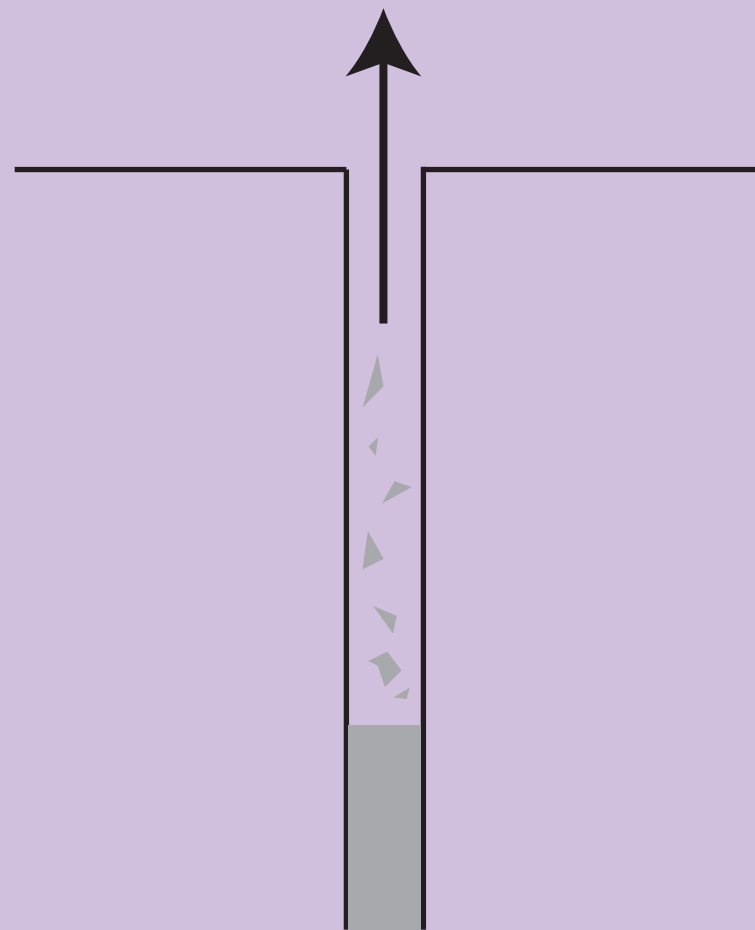
- line 826: ratio rather than ration.

*Changed*

- figure 10: in this figure pyroclasts all look like crystals (i.e. with no bubbles and with a rectangular shape). This could be misleading.

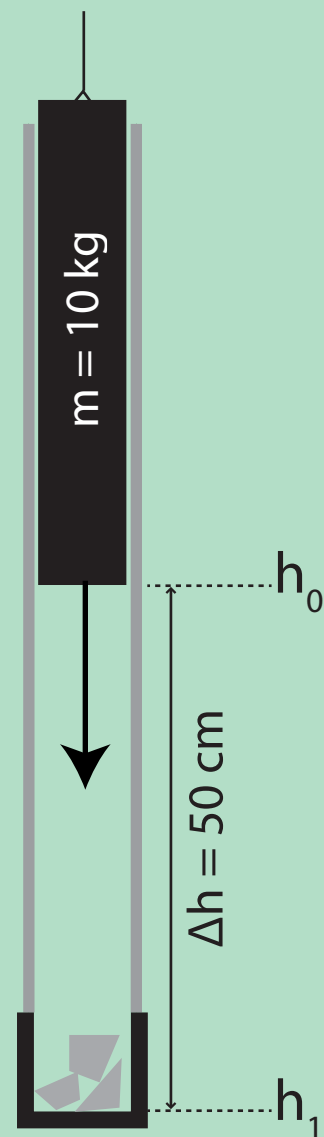
*Shapes have been altered to include more irregular shapes close to the fragmentation front.*

### Rapid Decompression (Shock Tube)

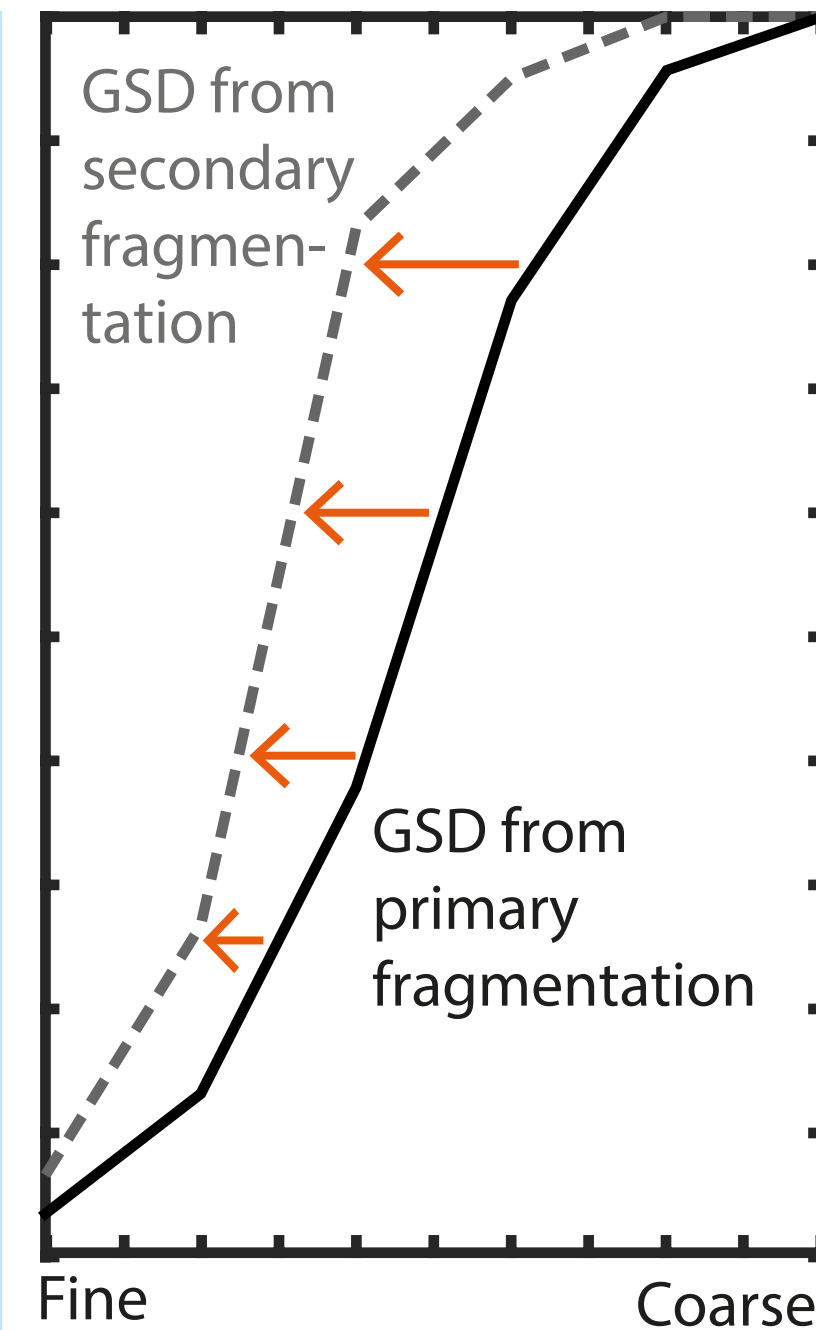
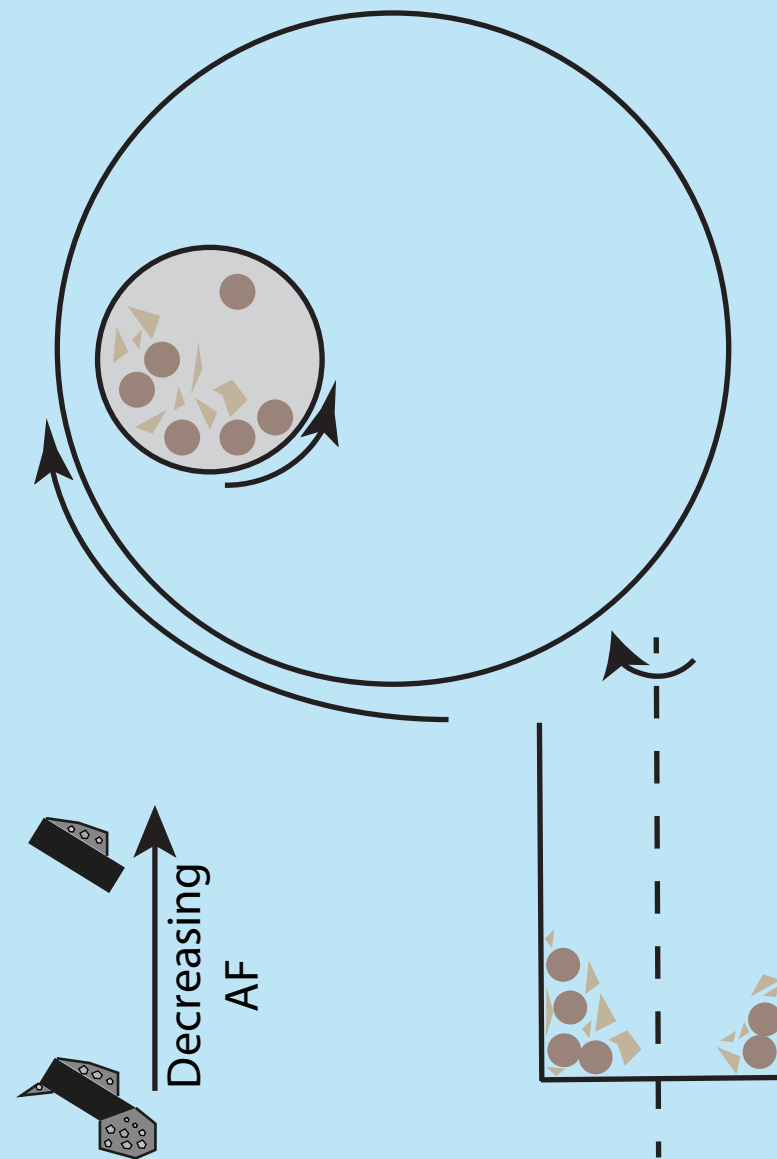


Temperature: 20°C or 880°C  
 Overpressure: 15MPa or 30MPa

### Impact (Falling Piston)



### Milling (Planetary Ball Mill)





**Highlights** [each bullet point - maximum 85 characters, including spaces. Max 5 points]

- We investigate ash production with decompression, impact and milling experiments
- Products follow fractal dimensions which are raised by secondary fragmentation
- We define a milling index (Adherence Factor) that quantifies the degree of abrasion
- Crystals provide a control on the GSD at certain size fractions
- Abrasion lowers grain axial ratio and strips adhering matrix from crystals

1  
2  
3  
4  
5  
6  
7  
8  
9  
10  
11  
12  
13  
14  
15  
16  
17  
18  
19  
20  
21  
22  
23  
24  
25  
26  
27

**Primary and secondary fragmentation of crystal bearing intermediate  
magma**

Thomas J. Jones<sup>1,2\*</sup>, Keri McNamara<sup>2</sup>, Julia Eychenne<sup>2</sup>, Alison C. Rust<sup>2</sup>, Katharine V.  
Cashman<sup>2</sup>, Bettina Scheu<sup>3</sup> and Robyn Edwards<sup>2</sup>

- [1] Department of Earth Sciences, Durham University, Durham, DH1 3LE, UK
- [2] School of Earth Sciences, University of Bristol, Wills Memorial Building, Bristol, BS8 1RJ, UK
- [3] Department of Earth and Environmental Sciences, LMU Munich, Theresienstr. 41, 80333 Munich, Germany

**\*Corresponding author:** [t.j.jones@durham.ac.uk](mailto:t.j.jones@durham.ac.uk)

## Abstract

28  
29 Crystal-rich intermediate magmas are subjected to both primary and secondary fragmentation  
30 processes, each of which may produce texturally distinct tephra. Of particular interest for volcanic  
31 hazards is the extent to which each process contributes ash to volcanic plumes. One way to address  
32 this question is by fragmenting pyroclasts under controlled conditions. We fragmented pumice  
33 samples from Soufriere Hills Volcano (SHV), Montserrat, by three methods: rapid decompression in a  
34 shock tube-like apparatus, impact by a falling piston, and milling in a ball mill. Grain size  
35 distributions of the products reveal that all three mechanisms produce fractal breakage patterns, and  
36 that the fractal dimension increases from a minimum of  $\sim 2.1$  for decompression fragmentation  
37 (primary fragmentation) to a maximum of  $\sim 2.7$  by repeated impact (secondary fragmentation). To  
38 assess the details of the fragmentation process, we quantified the shape, texture and components of  
39 constituent ash particles. Ash shape analysis shows that the axial ratio increases during milling and  
40 that particle convexity increases with repeated impacts. We also quantify the extent to which the  
41 matrix is separated from the crystals, which shows that secondary processes efficiently remove  
42 adhering matrix from crystals, particularly during milling (abrasion). Furthermore, measurements of  
43 crystal size distributions before (using x-ray computed tomography) and after (by componentry of  
44 individual grain size classes) decompression-driven fragmentation show not only that crystals  
45 influence particular size fractions across the total grain size distribution, but also that free crystals are  
46 smaller in the fragmented material than in the original pumice clast. Taken together, our results  
47 confirm previous work showing both the control of initial texture on the primary fragmentation  
48 process and the contributions of secondary processes to ash formation. Critically, however, our  
49 extension of previous analyses to characterization of shape, texture and componentry provides new  
50 analytical tools that can be used to assess contributions of secondary processes to ash deposits of  
51 uncertain or mixed origin. We illustrate this application with examples from SHV deposits.

52 **Keywords:** Volcanic ash; Fragmentation; Broken crystals; Milling; Fractals; X-ray computed  
53 tomography

54 **1. Introduction**

55 Volcanic ash is an inevitable product of nearly all explosive eruptions. Formed by fragmenting  
56 magma and/or rock, it is a particularly **important** hazard in the modern day, presenting a risk to  
57 aviation as well as to human health. Additionally, the associated risk is not confined to areas proximal  
58 to the volcano, but, as demonstrated by recent eruptions in Iceland and Chile, can also have far  
59 reaching impacts (e.g., Alfano et al., 2011). Understanding the origin of volcanic ash particles is thus  
60 critical for predicting the nature and extent of ash hazards. **Volcanic ash can form by both primary and  
61 secondary processes; the former from volatile-driven decompression during magmatic ascent and the  
62 latter from post-fragmentation processes such as collisions within the conduit and transport in  
63 pyroclastic density currents (PDCs). Distinguishing between the products of primary and secondary  
64 fragmentation is necessary for a comprehensive understanding of volcanic ash deposits.**

65

66 Primary magmatic fragmentation occurs either through ascent-driven vesiculation and expansion of a  
67 volatile phase or by rapid decompression, such as occurs because of edifice collapse. Typical  
68 fragmentation studies relate tephra characteristics (e.g., grain size distributions, GSDs) to the energy  
69 of the primary fragmentation (e.g. Walker, 1973). Secondary fragmentation further decreases the  
70 average grain size of a pyroclastic deposit. In PDCs, secondary ash-forming processes include both  
71 impact and abrasion (e.g. Freundt and Schmincke, 1992), which cause fining of vent-derived particles  
72 with increased transport distance (Dufek and Manga, 2008; Kueppers et al., 2012). The total grain size  
73 distribution (TGSD) produced by primary and secondary fragmentation processes, in turn, affects the  
74 efficiency of heat transfer (e.g., Zimanowski et al., 2003), PDC mobility (Félix and Thomas, 2004)  
75 and formation of co-PDC plumes (Eychenne et al., 2012). For this reason, identifying the  
76 contributions of co-PDC ash to the total deposit is particularly important for modelling ash plumes,  
77 especially in large eruptions where such deposits may make up a large proportion of distal ash (e.g.  
78 Darteville et al., 2002; Cashman and Rust, 2016; Engwell and Eychenne, 2016; Engwell et al., 2014;  
79 Eychenne et al., 2015; Eychenne et al., 2012; Rose and Durant, 2009). The goal of our work is to  
80 develop analytical tools to distinguish primary from secondary ash deposits.

81

82 Controlled laboratory experiments have provided some links between natural variables (e.g. degree of  
83 overpressure, transport distance) and the characteristics of the associated tephra deposit. Laboratory  
84 study of primary fragmentation is typically performed by shock-tube experimentation at magmatic  
85 temperatures. Results show that for a given sample porosity, greater degrees of overpressure increase  
86 the fragmentation efficiency and thus decrease the overall grain size (Kueppers et al., 2006b).  
87 Experimental GSDs typically follow power-law distributions with fractal dimensions (D) of ~2.5  
88 (Kueppers et al., 2006a). Variations about this value are thought to reflect the energy of  
89 fragmentation, with higher fragmentation energies producing deposits with higher D values (Perugini  
90 and Kueppers, 2012). The fractal dimension increases by secondary fragmentation (Kaminski and  
91 Jaupart, 1998). The effects of secondary fragmentation have been quantified using experiments  
92 involving both collision and abrasion (Cagnoli and Manga, 2004; Mueller et al., 2015). Results  
93 confirm that the fine ash content increases with time, and that experiments involving abrasion produce  
94 finer ash than experiments involving impact (Mueller et al., 2015). Also important is the original clast  
95 density, with grain size reduction dominated by breakage of the more vesicular fragments (Kueppers  
96 et al., 2012). This observation has particular relevance to explosively generated ash, which often has  
97 TGSDs dictated by the vesicle **size distribution** (Genareau et al., 2012; Liu et al., 2015a; Rust and  
98 Cashman, 2011).

99

100 Less well studied is the role of crystals in fragmentation and ash formation. Crystals commonly form  
101 a major constituent of intermediate magmas; thus it seems likely that the abundance and size  
102 distributions of crystals would affect the size, density and shape of explosively generated fragments.  
103 In fact, crystal concentrations in ash deposits show that individual crystals typically have a limited  
104 size and density range (e.g., Martel et al., 2001; Cashman and Rust, 2016; Sparks and Walker, 1977).  
105 Crystals in ash fractions are often broken or rounded, possibly due to the fragmentation and/or ash  
106 generation mechanism (e.g. Bachmann et al., 2002; Best and Christiansen, 1997; Carter et al., 1986).  
107 The presence of broken crystals in explosive eruption deposits has previously been attributed to two  
108 main processes: melt inclusion (MI) decrepitation and shock fragmentation. Fragmentation by MI  
109 decrepitation occurs when overpressure in the MI exceeds the tensile strength of the crystal. This may

110 be achieved by cyclic periods of overheating linked to the latent heat of crystallisation (Bindeman,  
111 2005; Zhang, 1998) or rapid decompression of crystal-bearing magma during ascent (Best and  
112 Christiansen, 1997; Bindeman, 2005; Miwa and Geshi, 2012; Tait, 1992; Williamson et al., 2010).  
113 Crystal fragmentation by shock fragmentation can occur by extensional fracture during  
114 decompression and subsequent melt vesiculation (Chouet et al., 1994; Kennedy et al., 2005; Miwa  
115 and Geshi, 2012; Pallister et al., 1996).

116

117 Here we present a multi-component analysis of experimentally fragmented pumice samples. Although  
118 the effects of both rapid decompression and abrasion have been previously investigated, we extend  
119 these experiments in several important ways. First, we focus on fragmentation of a vesicle- and  
120 crystal-rich intermediate magma by a range of methods. Second, we explore the effects of both  
121 primary and secondary fragmentation on the resulting shape, size and componentry of the particle  
122 population. Primary fragmentation is simulated by rapid decompression experiments in a shock tube  
123 while secondary processes (such as abrasion and impact in PDCs) are simulated in the laboratory by  
124 ball mill and falling piston experiments, respectively. Controlled experiments with the same starting  
125 material – pumice from recent eruptions of the Soufriere Hills Volcano (SHV) – allow us to compare  
126 the ash-generating efficiency of the **different** processes. Additionally, adding componentry analysis  
127 allows us to evaluate the extent to which (broken) crystals affect the grain size, shape and fractal  
128 dimension of the tephra deposit. Finally, we compare our experimental results with natural SHV ash  
129 samples from fallout deposits produced by a dome collapse and a Vulcanian eruption.

130

## 131 **2. Methods**

132 All experiments were conducted using a single crystalline andesite pumice block that survived  
133 decompression during an explosive (Vulcanian) eruption of SHV in February 2010. We fragmented  
134 the pumice sub-samples in three different ways: rapid decompression at both room temperature and  
135 880°C, impact and milling at room temperature - all within the brittle deformation field; (Alidibirov  
136 and Dingwell, 2000). To characterize the resulting material, we determined the total grain size  
137 distributions produced by each fragmentation method, as well as ash components, shapes and textures.

138 For the decompression experiments, we also compare crystal sizes and shapes before and after  
139 fragmentation.

140

## 141 *2.1 Pre-fragmentation characterisation*

142 The original sample had a dense-rock equivalent density of  $2.69 \times 10^3 \text{ kg m}^{-3}$  and an estimated glass  
143 transition temperature ( $T_g$ ) of  $\sim 790^\circ\text{C}$  (Jones et al., 2013). For the decompression experiments we  
144 drilled four pumice cylinders, each measuring 60 mm long and  $\sim 25$  mm in diameter. Prior to  
145 fragmentation the physical and textural properties were characterised. Crystal populations and pre-  
146 existing crystal fractures were quantified with X-Ray computed tomography (XRCT) and optical  
147 microscopy of thin sections; helium pycnometry was used to calculate connected and total porosities  
148 for the four samples (see Table 1).

149

### 150 *2.1.1 X-Ray computed Tomography*

151 Radiographs for XRCT were collected with a Nikon Meterology 225/320kV Custom Bay scanner  
152 located at the Henry Mosely X-Ray Imaging Facility, University of Manchester. Acquisition  
153 conditions were 41 kV accelerating voltage, 239  $\mu\text{A}$  current and a 0.5 mm Al filter. An exposure time  
154 of 1000 ms was used for all scans. To reconstruct the scans, we first calculated the centre of rotation  
155 of all the radiographs and then applied a beam hardening correction using the Xtek CT Pro software.

156

157 All processing was conducted using the 3D visualization and segmentation software Avizo 8.0  
158 Standard. Crystal volumes were determined from a sub-volume of  $\sim 2.5 \times 10^8$  voxels extracted from the  
159 raw image stack, where 1 voxel measures  $0.02257 \text{ mm}^3$ . A  $3 \times 3 \times 3$  voxel 3D median filter was applied  
160 to this sub-volume with three iterations. Each image in the stack was segmented and thresholded to  
161 identify phases based on their characteristic grey scale values. A binary data set was then created to  
162 generate either the surface or volume of the segmented crystals. Only objects of 5 voxels or larger  
163 were included in calculations of crystal volumes. The separation of pre-broken crystal fragments can  
164 be achieved when distances are  $> \sim 0.09 \text{ mm}$ .

165

166 Mineral modes, porosity and bulk sample crystallinity were determined with a larger sub-volume of  
167  $6 \times 10^8$  voxels, which required significantly more computational capacity than the crystal volume  
168 measurements, and therefore a different approach. Firstly a median filter was applied to the entire  
169 image stack with ImageJ software (<http://rsbweb.nih.gov/ij/>). Next pores and mafic and felsic mineral  
170 phases in each image were separated based on grey scale values with an ImageJ plugin, PhaseQuant  
171 (Elangovan et al., 2012). The small density variation between different mineral phases, and the  
172 corresponding similarity of grey scales, made segmentation of specific minerals difficult so crystals  
173 are classified as either mafic or felsic phases (e.g. Cnudde et al., 2006). Each segmented volume  
174 (felsic, mafic and pores) was then converted into a binary image stack and imported into Avizo. The  
175 felsic crystal data required a 3D erosion and subsequent dilation by two voxels to remove background  
176 noise. Finally, surface generation and volume analysis was performed.

177

### 178 *2.1.2 Textural characterisation*

179 A 3D rendered volume of an example sub-sampled volume (Figure 1a) shows the distribution of  
180 crystals prior to experimental fragmentation. Broken crystals are common, and often have a jigsaw-  
181 like fit. Where the separation between these crystal fragments was sufficient to resolve in the  
182 tomographic analysis, each crystal fragment was counted as a separate crystal. The average DRE  
183 crystallinity for crystals  $>32 \mu\text{m}$  in diameter ( $5 \phi$ ) is 27 vol. % with ~21% felsic and ~6% mafic  
184 crystals and oxides. Point counts of petrographic thin sections of the same samples included smaller  
185 microlites, and thus yield a higher crystallinity (38%); this shows that about 11% of the total crystal  
186 volume is  $< 32 \mu\text{m}$ .

187

188 A crystal volume distribution (CVD) extracted from the rendered tomographic volumes is shown in  
189 Figure 1b. The crystals range in size from  $10^{-5}$  to  $10^1 \text{ mm}^3$ , with a mode of  $10^{-3} \text{ mm}^3$ . Measurement of  
190 broken crystals as individual fragments means that the rendered volume distribution accounts for pre-  
191 existing crystal breakage prior to experimental fragmentation, within the resolution of the imaging  
192 technique.



193

### 194 2.3 Porosities and fragmentation threshold

195 Porosity provides information about the potential energy available for fragmentation during  
196 decompression (Kueppers et al., 2006b) and is used to calculate the minimum initial overpressure  
197 required for complete fragmentation in the decompression experiments (Spieler et al., 2004). To  
198 measure porosity, we cleaned the sample cores and measured their porosity by helium pycnometry,  
199 using a Quantachrome Instruments Ultrapync 1200e pycnometer housed at LMU Munich, Germany.

200 Total porosity  $\phi_{\text{total}}$  was calculated from the solid density  $\rho_{\text{solid}}$  and the bulk sample density  $\rho$  as:

$$201 \quad \phi_{\text{total}} = 1 - \frac{\rho}{\rho_{\text{solid}}}, \quad [1]$$

202 where  $\rho_{\text{solid}}$  is the measured density of powdered sample milled to a grain size less than the minimum  
203 pore size. The connected or open porosity  $\phi_{\text{open}}$  is calculated as:

$$204 \quad \phi_{\text{open}} = \left( \frac{V_C - V_M}{V_C} \right) \times 100, \quad [2]$$

205 where  $V_C$  is the geometrical volume of the cylindrical samples and  $V_M$  is the volume measured by He  
206 pycnometry. The isolated (closed) porosity,  $\phi_{\text{closed}}$  can then be defined as:

$$207 \quad \phi_{\text{closed}} = \phi_{\text{total}} - \phi_{\text{open}}. \quad [3]$$

208

209 The average total porosity is 66%, with a range of 1.25% between all sample cores. Individual  
210 porosity values for the cores used in the four rapid decompression experiments are reported in Table  
211 1.

212

### 213 2.2 Experimental fragmentation

214 Samples from the Soufriere Hills Volcano (SHV) were fragmented experimentally by three methods:  
215 rapid decompression, hammer impacts and ball milling (Figure 2). Broadly, these aimed to replicate  
216 three natural volcanic processes: magmatic overpressure and decompression, impact and abrasion/  
217 milling in turbulent flow.

218 Rapid decompression-driven fragmentation was performed using a shock tube-like apparatus  
219 (Figure 2a) at the LMU Munich, Germany (e.g. Scheu et al., 2008; Spieler et al., 2004). By using two

220 experimentally calibrated diaphragms we achieved a pressure differential of either 15 or 30 MPa; this  
221 exceeds the fragmentation threshold by 12 and 27 MPa (Spieler et al., 2004). At each differential  
222 pressure, experimental fragmentation was conducted at both 20°C and 880°C. The experimentally  
223 generated pyroclasts were left to settle in the low pressure tank for 1-2 hours and then sieved to 125  
224 µm using a pressure washer filled with distilled water. All material that passed through the 125 µm  
225 sieve was left to settle for 2 days in a sediment collection tank.

226 Impact experiments were performed by placing a single rectangular block (~ 4 x 5 x 2cm) of  
227 SHV pumice into a detachable steel cup, as illustrated in Figure 2b. A 10 kg steel piston was then  
228 repeatedly dropped from a height of 50 cm. The five experimental runs, each run with a different  
229 block, comprised 5, 10, 15, 20 and 25 piston drops; at the end of each run the entire sample was  
230 recovered from the basal cup by flushing with distilled water.

231 Ball mill grinding was performed using a Planetary Ball Mill PM 100 manufactured by  
232 RETSCH Ltd. The initial GSD for the ball mill experiments, represented by “0 min” in Figure 3c, was  
233 created by crushing ~ 10cm square blocks of SHV pumice. For each experiment an aliquot of this  
234 input sample was weighed and placed into the agate jar of the ball mill (Figure 2c) along with six 1.6  
235 cm diameter agate balls. The container was sealed and rotated at 450 rpm for 0.5, 1, 2.5 or 5 minutes,  
236 and the sample removed for subsequent analysis.

237

### 238 *2.3 Post-fragmentation characterisation*

239 After fragmentation by the three methods (Figure 2) the experimental pyroclasts were  
240 characterised by grain size, componentry, shape and fracture surface morphology.

241

#### 242 *2.3.1 GSD measurements*

243 All particles coarser than 125 µm were separated into grain size fractions by manual sieving  
244 into size bins of -3, -2, -1, 0, 1, 2, 3 phi (φ). Particle size analysis for material ≤ 250 µm was  
245 performed at the Environmental Change Laboratory, University of Western England, Bristol, UK  
246 using a Mastersizer 2000 laser diffraction particle size analyser, manufactured by Malvern

247 Instruments Ltd. Sieve and Mastersizer data were combined using the overlapping 3  $\phi$  size fraction to  
248 produce a total grain size distribution for each fragmentation experiment.

249

### 250 *2.3.2 Componentry*

251 Componentry analysis was conducted under a binocular microscope for grain sizes -3 to 3  $\phi$ .  
252 Grains  $\geq 500 \mu\text{m}$  were picked manually; smaller grains were classified from analysis of digital  
253 microscope images. Where possible, at least 300 grains were analysed for each grain size fraction.  
254 Grains were separated into three component categories: (1) free mafic crystals, (2) free felsic crystals,  
255 and (3) clasts (i.e. anything that is not a free crystal), where a free crystal is defined as having matrix  
256 adhered to less than 20% of the surface of the crystal. Additional 2D componentry of the 2  $\phi$  ash  
257 fraction was performed using backscattered electron (BSE) mode of Scanning Electron Microscopy  
258 (SEM) on a Hitachi S-3500N SEM at the School of Earth Sciences, University of Bristol. This grain  
259 size fraction was chosen for detailed analysis because all experiments produce sufficient samples of  
260 this size fraction. Ash grains were set in resin and polished to expose grain interiors before being  
261 carbon coated. A mosaic of 25 images was taken of each sample using BSE mode from a working  
262 distance of 18 mm, a 15Kv accelerated voltage and a magnification of 60x. Each image had a 1024 x  
263 768 pixel resolution. Componentry was performed manually by placing a grid on the image and  
264 counting grains. Grains were subdivided into three components: (1) crystals with no attached matrix,  
265 (2) crystals with matrix attached, and (3) vesicular matrix clasts (all matrix grains were vesicular).

266 The 3D morphology of fine ash samples was examined using **secondary electron mode on the**  
267 SEM. Ash grains within the 2  $\phi$  sieve fraction were mounted on carbon-based stubs and Au coated to  
268 a thickness of approximately 5 nm. For grains measuring 125-250  $\mu\text{m}$  or 3  $\phi$  (the finest fraction  
269 studied), silver paint was applied to the SEM stub prior to Au coating, to reduce the effects of  
270 charging.

271

### 272 *3.2.3 Shape analysis*

273 The 2D SEM image mosaics of the 2  $\phi$  grain size fraction were analysed with ImageJ  
274 software. Images of individual grains were thresholded and converted to binary format before

275 quantifying grain shapes using axial ratio and convexity. Only grains from the ‘vesicular matrix’  
 276 componentry category were analysed for shape as they displayed the most variation between sample  
 277 runs. This component comprised between 10 and 60 % of the total depending on the fragmentation  
 278 mechanism.

279 Axial ratio is the ratio of the axes of the particle’s best-fit ellipse:

280 
$$\text{Axial Ratio (AR)} = \frac{\text{Major Axis Length}}{\text{Minor Axis Length}}. \quad [4]$$

281 Convexity is defined as the ratio of the perimeter of the grain and its convex hull (the smallest convex  
 282 polygon that contains the 2D shape):

283 
$$\text{Convexity} = \frac{\text{Perimeter of Convex Hull}}{\text{Perimeter of Grain}}. \quad [5]$$

284 It is a measure of the surface roughness of the external shape boundary (Liu et al., 2015b), such that a  
 285 high value of convexity indicates a smooth external surface.

286 Where a crystal comprised at least 10% of the entire grain, areas of crystals and matrix were also  
 287 calculated separately by manually varying the greyscale threshold to generate separate binary images,  
 288 then calculating the pixel area of each. Abrasion is expected to decrease the relative proportion of  
 289 glassy matrix adhering to crystals. For this reason, Meyer (1971) define the “abrasion index”, which is  
 290 the ratio of the area of a crystal to the area of attached matrix. However, abrasion may not be the only  
 291 process to affect the crystal-matrix ratio. Furthermore, Meyer’s “abrasion index” is unbounded (i.e.  
 292 becomes infinite if there is no matrix). For these reasons, we introduce a related parameter we call the  
 293 Adherence Factor:

294 
$$\text{Adherence Factor (AF)} = \frac{\text{Area of Crystal}}{\text{Area of Crystal} + \text{Area of Attached Matrix}} \quad [6]$$

295 The adherence factor is bounded between one (matrix only with no dominant crystal) and zero (for a  
 296 crystal with no adhered matrix) and therefore we expect AF to decrease with increasing abrasion.

297 **4. Results**

298 *4.1 Grain size distributions*

299           The grain size distributions (GSD) of all sample sets are limited to a maximum of  $-3\phi$  because  
300 of initial sample size. Rapid decompression (Figure 3a) creates a sample suite with a median size of -  
301  $2.30\phi$  to  $0.23\phi$ . Most striking is the effect of changing fragmentation temperature, where elevated  
302 temperatures yield coarser GSDs. The grain size distributions produced from the falling piston  
303 experiments are notably more fine-grained than pyroclasts produced by rapid decompression. Median  
304 sizes range from  $1.70\phi$  to  $5.03\phi$  and generally decrease with increased number of hits (Figure 3b).  
305 The grain size resulting from 10 hits, however, is abnormally small relative to the other data sets; we  
306 attribute this to natural heterogeneity within the pumice block that was the source of the starting  
307 material of each experiment. Experimentally generated pyroclasts from ball milling show a systematic  
308 increase in fine particles with increased milling duration. All GSDs produced by milling show a  
309 pronounced fine tail and are skewed to smaller sizes than GSDs from the rapid decompression and  
310 falling piston experiments.

311

312 *4.2 Ash shape*

313           Vesicular grains (i.e. all those that were not dominated by a single large crystal of over 10%  
314 of the total grain) were analysed for two shape parameters: axial ratio and convexity. Axial ratio is a  
315 representation of particle elongation, while convexity quantifies the smoothness of the grain exterior  
316 (Liu et al., 2015b). Axial ratio values vary considerably depending on the experimental fragmentation  
317 method (Figure 4a-c). Ash produced by rapid decompression has a greater range of axial ratio values  
318 than those produced by milling or impact. Ash grains from the milling experiments showed the  
319 smallest range of axial ratios although the range increased with milling time: axial ratios of grains  
320 milled for 1 minute have a lower mode and extend to larger values than axial ratios of grains milled  
321 for 0.5 minutes (Figure 4c). In contrast, axial ratio values changed little with number of impacts  
322 (Figure 4b). However, convexity data show that increased impacts smoothed out the irregular grain  
323 surfaces in the comparative grain size fraction: the ash grains produced by 10 piston impacts have  
324 greater average convexity values, and thus less irregular exteriors, than grains produced by 5 impacts  
325 (Figure 4e).

326

#### 327 *4.3 Experimentally generated pyroclast componentry*

328 Componentry analysis of the pyroclasts generated by rapid-decompression required the proportions of  
329 free mafic and felsic crystals (those with < 20% adhered matrix) to be discriminated from other matrix  
330 dominated clasts (Figure 5a). No free crystals were observed at grain sizes greater than  $-1 \phi$ . At finer  
331 grain sizes the proportion of crystals varies considerably for different grain size fractions. Within  
332 these coarse-grained rapid decompression products, free crystals (mainly felsic) are most abundant in  
333 the  $1\phi$  size fraction, contributing  $\sim 40$  weight % to this grain size bin. The maximum abundance of  
334 mafic crystals varies between  $1$  and  $2 \phi$  for different experimental runs. We observed no systematic  
335 componentry changes in the decompression experiments (Fig. 5a) as a function of either  $\Delta P$  or  
336 fragmentation temperature; the small variations between experimental runs likely relate to slight  
337 sample heterogeneities prior to experimental fragmentation.

338

339 Within the  $2\phi$  fraction (Fig. 5b), there are only small differences in SEM componentry between the  
340 hot and cold rapid decompression products. Both have similar proportion of free crystals (with no  
341 attached matrix) although there is a higher proportion of crystals with attached matrix in the products  
342 of hot decompression (Figure 5b). More dramatic is the comparison with data from other  
343 fragmentation mechanisms, where products of the milling and impact experiments show a higher  
344 proportion of free crystals than the decompression products. Additionally, the sample milled for  
345 longer (1 min) has a higher proportion of free crystals than its counterpart that was milled for 30  
346 seconds. A similar trend is observed in the impact products: the sample that underwent 10 hits has a  
347 greater proportion of free crystals than the sample that was hit five times. **These observations show**  
348 **that repeated fragmentation removes crystal coatings and frees individual crystals from the matrix.**

349

#### 350 *4.4 Crystal volume distributions*

351 The crystal populations within the original SHV pumice cores and the pyroclasts produced by rapid  
352 decompression were quantified by analysis of X-Ray CT (Figure 1) and SEM analysis (Figure 5a),  
353 respectively. To effectively compare these pre-experiment and post-experiment crystal populations,

354 the crystal volume distributions generated by X-Ray-CT were converted to a length scale. We assume  
355 that all crystals within the volcanic rock samples form euhedral cuboid volumes,

356 
$$V_{\text{cuboid}} = h \times w \times l \quad [7]$$

357 where  $h$  and  $w$  represent the height and width of the smallest crystal face and  $l$  is length. Assuming  
358 that crystals have aspect ratios of 2:1 and that the minor and intermediate axes are the restrictive  
359 dimensions of the sieve size ( $d$ ), an effective particle diameter is calculated as:

360 
$$d = \left( \frac{V_{\text{cuboid}}}{2} \right)^{1/3} \quad [8]$$

361 Effective diameters are converted to the  $\phi$  scale, the volumes falling in each  $\phi$  bin summed and  
362 converted to weight % to form the “Rock” data set in Figure 6.

363

364 The crystal population generated by decompression is determined by averaging the mass of  
365 mafic/felsic crystals within each size fraction of all decompression experiments. We average because  
366 no significant difference in componentry was observed when changing fragmentation overpressure or  
367 temperature. These data are then converted to weight % of total crystals and form the “Ash” data set  
368 in Figure 6.

369

370 The size distribution of crystals within the ash relative to those in the SHV pumice (Figure 6) shows  
371 that rapid decompression caused the crystal size to decrease. Grain size reduction is concentrated  
372 over the central portion of the size range investigated. In coarser grain size fractions ( $2 - 0 \phi$ ) the  
373 crystal abundance in the pumice is greater than the abundance in the ash and is dominated by felsic  
374 crystals. Conversely, in the finer fractions ( $1 - 3 \phi$ ) crystals are more abundant in the ash than in the  
375 original pumice. Moreover, there are no crystals within the  $-2\phi$  ash fraction, although they were  
376 present in the pumice prior to decompression and fragmentation. This suggests that crystals were not  
377 simply freed from the matrix during fragmentation but were also reduced in size by crystal breakage.

378

379 *4.5 SEM imagery of fracture surfaces*

380 Photomicrographs of the 2 $\phi$  ash fraction produced by rapid decompression reveal characteristics of  
381 broken crystal surfaces (Figure 7) that can be classified as: (1) smooth, clean surfaces with negligible  
382 topographic relief (Figure 7a) and (2) rougher, often highly irregular surfaces displaying intense river-  
383 line fracturing and hackles (Figures 7c and 7d). On some crystals, a vesicular glass coating is  
384 observed (Figure 7b); it is slightly more common in the hot fragmentation experiments relative to the  
385 room temperature runs. No other differences were observed in the fracture surfaces or styles between  
386 the products of hot and cold experiments. About 90% of broken crystals have clean broken surfaces  
387 with negligible topographic relief. We interpret these as breakage along a cleavage plane or a pre-  
388 existing internal fracture (Figure 7a). Where river-line fractures are observed on these surfaces they  
389 are widely spaced and have low relief. Only about 10% of broken crystal surfaces are much rougher  
390 and complex due to fractures cross-cutting cleavage planes (e.g. Figure 7d).

391

392 Finally, sub-circular cavities, including some with protruding glass strands, are a rare but ubiquitous  
393 feature of crystal surfaces in the experimental products. Similar features were observed by  
394 Williamson et al. (2010) in natural SHV pumice and interpreted as melt inclusions that burst within a  
395 plastic groundmass due to a major decompression event (e.g. dome collapse). Melt extension is a  
396 non-brittle process that could not have been generated through experimental fragmentation at room  
397 temperature. The fact that we observe these features in the experiment products indicates that they  
398 must already have existed in the dome/pumice samples prior to decompression in the laboratory.

399

## 400 **5. Discussion**

401 We have explored several techniques to characterise both experimentally generated ash and its parent  
402 material (Table 1). We now use these results - from grain size measurements, fractal analysis,  
403 componentry and shape descriptors - to examine the effects of different fragmentation mechanisms on  
404 pyroclast characteristics. For samples that were rapidly decompressed, we couple this analysis with  
405 XRCT and SE SEM imagery to examine how rapid decompression-driven fragmentation alters the  
406 crystal population. Lastly, to illustrate our techniques we compare experimentally generated SHV ash  
407 to two natural SHV ash examples.



408

409 *5.1 Fractal behaviour of products*

410 Since the idea of fractal behaviour was introduced to Earth Sciences (e.g., Korvin, 1992; Turcotte,  
411 1986), power law exponents (fractal dimension D values) have been used to quantify the size  
412 distributions of volcanic pyroclastic products (e.g., Kaminski and Jaupart, 1998; Perugini et al., 2011;  
413 Taddeucci et al., 2004). Higher power law exponents represent tephra deposits that are dominated by  
414 finer ash fractions. Therefore fractal dimensions are commonly used to infer the fragmentation  
415 efficiency and have been linked to the energy available for fragmentation (e.g., Kueppers et al.,  
416 2006a).

417

418 It has long been noted that tephra produced from volcanic eruptions commonly has a much higher  
419 fractal dimension (larger fine ash component) than expected from simple crushing or rock  
420 disaggregation (Hartmann, 1969). The source of this fine ash is an open question, but is clearly  
421 dictated ultimately by the vesicle size distribution (Rust and Cashman, 2011). Kaminski and Jaupart  
422 (1998) proposed a model of secondary fragmentation based on experimental fragmentation, where  
423 they assumed that piston impact causes primary fragmentation while grinding in a ball-mill caused  
424 secondary fragmentation. In this scenario, primary fragmentation initially creates  $D=2.5\pm 0.1$ , then  
425 ongoing selective re-fragmentation through particle-particle collisions increases the values of  $D \geq 3$   
426 preserved in fall deposits. However, many experimental fragmentation experiments fail to replicate  
427 the high power law exponents observed in natural pyroclastic deposits (Table 2). This leads to a  
428 question about the mechanism(s) capable of producing the finer ash, particularly the role of the  
429 original bubble population in controlling the final grain size distribution (Rust and Cashman, 2011).

430

431 We analysed the fractal dimension of the total GSD for all experimental fragmentation methods by  
432 converting raw data (mass proportion of particles in different size bins; Figure 3) to number-based  
433 data to aid comparison to other published data sets (e.g. Kueppers et al., 2006a). Over the size range  
434 analysed here, all experimentally produced ash samples follow a power law distribution, that is, they  
435 plot on a straight line in  $\log(N)$ – $\log(L)$  space (Figure 8), where N represents the number of grains

436 larger than corresponding fragment size ( $L$ ) and the slope defines the fractal dimension ( $D$ ). The  
437 power-law distributions were fitted to the total GSD recovered from the experiments. In some cases  
438 one or two data points are excluded at the coarse or fine tail (open circles in Figure S1).

439

440 The  $\log(N)$  vs.  $\log(L)$  data for the rapid decompression experiments (Figure 8a) form linear trends  
441 with fractal dimensions between 2.03 and 2.24, in good agreement with other studies that have used  
442 the same fragmentation method (Kueppers et al., 2006a; Kueppers et al., 2006b; Perugini and  
443 Kueppers, 2012). Pyroclasts from the impact (falling piston) experiments also show a fractal  
444 distribution (Figure 8b) with a mean  $D = 2.60$ . This value is comparable to values from simple  
445 crushing and disaggregation of rocks (Table 2; Hartman, 1969). The falling piston sample set shows  
446 the most variation. Here  $D$  values do not vary systematically with number of impacts, although the  
447 power law exponents do broadly increase with increased number of impacts. In these analyses, we  
448 excluded the tails of the fragment size distribution when calculating  $D$  (represented as open circles in  
449 Figure S1), which may account for minor disparities. The milling experiments follow a power law  
450 distribution, which shows a systematic increase in  $D$  from 2.33 at 0.5 min to 2.45 at 5 mins (Figure  
451 8c). This progressive rise in  $D$  suggests that milling not only creates fine ash but also causes the fine  
452 ash component to become increasingly dominant in the TGSD.

453

454 Our experimental data show that secondary fragmentation can progressively increase  $D$  from an initial  
455 value resembling rapid decompression-driven fragmentation to higher values. Yet, even after  
456 considerable milling durations (5mins) or a large number (25) of successive impacts, the experimental  
457 products do not exceed  $D$  values of 3. Furthermore, analysis of the  $2\phi$  fraction shows that the crystals  
458 were not being broken through milling, rather they were being stripped of adhering groundmass. This  
459 suggests that during secondary fragmentation of crystal rich tephra, the crystal population may help to  
460 sustain a relatively coarse control on the GSD. This interpretation is supported by data from eruptions  
461 of Heimaey, Fuego and Oshima, where the basaltic pyroclasts are rich in microphenocrysts and the  
462 TGSDs have fractal dimensions  $D \sim 1.9-2.3$ . Silicic deposits (Mount St. Helens, El Chichon and  
463 Quizapu), in contrast, have both low (or no) groundmass crystallinity and  $D$  values  $>3$  (Table 2).

464 Assuming all of the eruptions listed in Table 2 involved secondary, as well as primary, fragmentation  
465 (through both milling and impacts, either with the conduit wall or within the particle-rich plume at  
466 depth), the differences in observed D seem most easily explained by variations in groundmass  
467 crystallinity. Where large proportions of crystals are present in the starting magma they provide a  
468 coarse control on the grain size distribution and prevent production of high proportions of fine ash;  
469 this keeps D values low ( $< 3$ ). The ‘final’ D value is therefore a function of both magma and  
470 fragmentation characteristics, including magma porosity and permeability, magma crystallinity,  
471 fragmentation overpressure and the degree of mechanical processing.

472

### 473 *5.2 Fragmentation control on pyroclast characteristics*

474 Our analysis confirms results from previous experimental studies, including the effect of mechanical  
475 fragmentation in shifting the GSD to smaller sizes (Cagnoli and Manga, 2004; Kueppers et al., 2012;  
476 Mueller et al., 2015) and the high efficiency of abrasion relative to impact experiments in producing  
477 fine ash (Mueller et al., 2015; Figure 3). We also found that the proportion of vesicular fragments  
478 decreased with increased milling time and number of impacts (Figure 5b), consistent with Kueppers et  
479 al. (2012).

480 Our experiments also show that the mechanism of fragmentation has a significant effect on the  
481 characteristics of individual pyroclasts. Of particular note is the variation in the axial ratios of matrix  
482 fragments between the three fragmentation mechanisms studied (Figure 4). The axial ratios of impact  
483 and milling products are large compared to the decompression products, which suggests that increased  
484 mechanical abrasion prevents, or rapidly reduces, the likelihood of producing elongated fragments.  
485 Additional milling further increases the mean and range of axial ratio values of ash particles. This is  
486 interesting because the small ash particles mimic shape variations previously observed in larger  
487 pumice clasts, both in rock tumbling experiments and natural PDC deposits (e.g., Manga et al., 2011).  
488 Studies of pumice clast rounding further suggest that both rounding and ash production via  
489 comminution are most efficient proximal to volcanic vents, where PDCs are most energetic.

490 A sizeable portion of the experimental products includes crystals with adhered matrix (Fig. 5b). Past  
491 studies have used these fragments as a marker for the amount of abrasion (Freundt and Schmincke,  
492 1992; Meyer, 1971). We quantified this effect using an ‘Adherence Factor’ (AF: Equation 6; Figure  
493 9). Our data show that the decompression experiments have a substantially higher AF (more adhered  
494 matrix) than the products of impact and milling. Hot decompression causes particles to retain slightly  
495 more matrix material than cold decompression. Interestingly, increasing the number of impacts or  
496 time of milling does not appear to dramatically alter the AF, but the products of milling have a lower  
497 AF, overall, than the products of impact.

498 To interpret the mechanisms responsible for adhered matrix produced by different fragmentation  
499 methods, it is also important to consider the effect of crystal breakage on AF. We identified broken  
500 crystals by recording whether the crystal displayed at least one intact ring of zoning or whether the  
501 zoning was interrupted. In the products of rapid decompression, the crystals with a lower AF value  
502 were typically broken. However, there is no obvious correlation between crystal breakage and AF in  
503 the products of milling and impacts (Figure S2); **this lack of correlation may be due to these two**  
504 **mechanisms not dramatically increasing the number of broken crystals.** As a consequence, the matrix  
505 is stripped from the outside without breaking the crystal, resulting in many whole crystals with a low  
506 AF value. In contrast, the low AF of broken crystals within products of rapid decompression suggests  
507 that, as crystals break, internal crystal surfaces are exposed and the area of adhered matrix decreases.  
508 Therefore we suggest crystal breakage is the main mechanism for reducing AF during rapid  
509 decompression.

510

### 511 *5.3 The influence of crystals on fragmentation during rapid decompression*

512 Crystals commonly form a major constituent of erupting magmas and there is the potential for the  
513 abundance and size distributions of crystals to affect the size, density and shape of fragments  
514 generated in explosive eruptions. The componentry analysis presented here demonstrates that free  
515 crystals contribute a significant mass (up to 40%) to specific grain size fractions produced by rapid  
516 decompression (Figure 5a). The size range in which crystals dominate appears independent of

517 fragmentation pressure and temperature and is directly related to the crystal size distribution in the  
518 starting material. Over the grain size range studied ( $-3$  to  $3 \phi$ ), plagioclase dominates the total crystal  
519 population within each size fraction of the experimentally generated fragments. This agrees with  
520 modal analysis of the starting material that showed it to be the most abundant mineral. As illustrated  
521 in Figure 5a, free crystals are non-existent or of trivial abundance in the grain size fractions coarser  
522 than  $0 \phi$ , consistent with the initial crystal size population in the starting material (Rock curve in  
523 Fig.6). The mafic crystals show a broader peak at smaller grain sizes, which is likely related to the  
524 initial size populations. Therefore the textural characteristics of the starting volcanic material (magma  
525 analogue) directly control the experimentally produced tephra (PDC analogue).

526

527 High proportions of crystals within a grain size fraction have the potential to alter the bulk ash  
528 density, especially at coarser grain sizes. This, in turn, will cause differential settling of crystals  
529 relative to glass fragments of similar size, particularly if the glass is vesicular (e.g., Sparks and  
530 Walker, 1977). This effect has been documented in natural eruptive products of Mount St Helens and  
531 Quizapu (Cashman and Rust, 2016), where the proportion of free crystals decreases faster with  
532 distance from the vent than pumice or glass shards from the same eruption. Currently, ash dispersion  
533 models (e.g. Tephra 2; Bonadonna et al., 2010) commonly use a single vesicular glass ash density to  
534 represent all grain size fractions from a volcanic eruption. Improvements could therefore be made to  
535 more accurately represent crystal-rich pyroclasts, particularly in eruptions characterised by PDCs.

536

537 Crystal size distributions may also help to explain the production of crystal pyroclasts devoid of glass  
538 coatings. If a whole (micro)phenocryst were to be extracted from the fragmenting magma, the surface  
539 would likely be at least partially coated in a glass. However, if internal broken fragments of a once  
540 larger phenocryst are extracted, then the relative chance of a glass-coated surface is low. **Knowing the  
541 surface properties of ash has implications for remote sensing applications and surface leachate studies.**  
542 Our componentry study suggests that free crystals in the ash generated by rapid decompression  
543 represent broken fragments from once larger whole crystals; this is likely because during rapid

544 decompression fragmentation, the crystals cannot accommodate deformation and hence fracture  
545 (Cordonnier et al., 2009).  
546  
547 Crystal fracture topographies indicate that breaking of crystals in our decompression experiments was  
548 dominantly along cleavage surfaces (type 1 fractures) with only about 10% of fractures cross-cutting  
549 cleavage planes (Figure 7). Crystals tend to break or ‘cleave’ along a particular crystallographic  
550 orientation because cleavage planes have a relatively low surface energy (Hull, 1999; Kelly and  
551 Macmillan, 1986). Experimental studies and natural observations of plagioclase identify intra-  
552 crystalline fractures controlled by crystallography and preferential fracture along cleavage planes (e.g.  
553 Borg and Heard, 1970; Brown and Macaudière, 1984). Further, Kennedy et al. (2005) use fractures in  
554 SHV hornblende crystals to infer the orientation of tensile unloading and therefore the shape of the  
555 fragmentation front. Under mode I tensile failure, cleavage surfaces have a direct and primary effect  
556 on fragmentation behaviour. When cleavage planes are orientated perpendicular to the tensile force  
557 (parallel to the unloading wave) then simple cleavage fracture is expected to occur (e.g., Figure 7a).  
558 However, when cleavage planes are orientated obliquely to tensile forces, then mode II failure can aid  
559 fracture by the formation of shear couples (Figure 7c). Therefore, the orientation angle, defined as the  
560 angle between the cleavage plane and the tensile force vector, will influence the relative proportions  
561 of mode I and II failure.

562

#### 563 *5.4 Comparison with natural samples*

564 **To compare with our experimental results, we also studied two ash samples from fallout deposits**  
565 **produced by a dome collapse event (on 31 March 1997) and a Vulcanian eruption (on 26 September**  
566 **1997) of Soufriere Hills Volcano. The dome collapse event generated PDCs but no plume at the vent,**  
567 **making the fallout deposit entirely co-PDC in origin (Bonadonna et al., 2002; Engwell and Eychenne,**  
568 **2016). The Vulcanian eruption produced both an eruptive column at the vent and PDCs on the**  
569 **volcano’s flank; the fallout deposit consequently includes ash from both vent-derived and co-PDC**  
570 **plumes (Bonadonna et al., 2002). These two natural events, with distinct eruption characteristics,**  
571 **allow us to demonstrate how our analysis techniques can be used on natural material to identify**

572 secondary fragmentation. To compare with experimental samples, we analysed the componentry, AF  
573 (Figure 9) and proportion of broken crystals in the 2  $\phi$  grain size fraction (Figure S2) of each sample.

574 The 2  $\phi$  fraction of both natural samples comprises approximately 30% dense material (crystals,  
575 phenocrysts and vesicle-free glass). The Vulcanian sample however, contains 15% crystals with  
576 adhered glass whereas the dome collapse sample contains approximately 20% (Figure 10). Hence the  
577 Vulcanian sample comprises approximately 55% vesicular fragments, while the ash produced by  
578 dome collapse contains less than 50%. Of this vesicular portion, the Vulcanian sample is comprised  
579 mostly of microlite-free vesicular glass fragments. In comparison, the dome collapse sample is  
580 comprised entirely of the microlite-rich vesicular glass. The higher proportion of vesicular microlite-  
581 free glass in the Vulcanian sample indicates that in addition to microlite-bearing magma stored at  
582 shallow levels (top of the conduit or dome), deep magma was erupted in the Vulcanian explosion. In  
583 contrast, the dome collapse event involved only material previously extruded in the dome, comprising  
584 microlite-rich glass of variable vesicularity. The two natural samples also differ in patterns of matrix  
585 adherence. The AF distribution of the Vulcanian sample is trimodal, with a major mode at AF ~0.2  
586 (low adhering matrix) and two minor modes at AF ~0.6 and 0.8 (Figs. 9 and S2). In comparison, the  
587 dome collapse sample shows a uniform AF distribution (Figure 9) and a higher proportion of broken  
588 crystals at low AF values (Figure S2).

589 Although this natural case study is illustrative only, and uses a single grain size fraction at a single  
590 location for each eruption, both the components and the AF distributions are distinctive. The  
591 differences in componentry (vesicle and microlite content) of the natural samples can be explained by  
592 the fact that they experienced different ascent and fragmentation histories and different transportation  
593 modes (PDCs vs. plumes); both of which should affect the mechanical properties. The Vulcanian  
594 sample includes both particles transported directly in a plume and particles that were first transported  
595 in PDCs before being entrained into co-PDC plumes. These two events can be observed, respectively,  
596 in Figure 9 as a group of poorly abraded particles (high AF values) and a set of highly abraded  
597 particles (low AF values). The dome collapse sample is dominated by microlite-rich particles that  
598 were entirely transported in PDCs. The uniform AF distribution suggests that abrasion during

599 transport did not affect all the phenocrysts uniformly. Differences might reflect: (1) the robustness of  
600 particles due to their high microlite content and moderate vesicularity compared to the highly  
601 vesicular, microlite-free particles produced by the Vulcanian eruption; and/or (2) the coarser initial  
602 grain size distribution in the dome collapse block-and-ash flows compared to the explosively  
603 produced Vulcanian pumice flows, whereby larger initial particle sizes would require more abrasion  
604 to release phenocrysts from the matrix. **This points to a limitation of our analysis, which is that we**  
605 **have not attempted to assess variations as a function of time/distance. At Tungurahua volcano, it has**  
606 **been suggested that dense crystal-rich PDCs become increasingly crystal rich with time/distance as**  
607 **the vesicular material is removed through abrasion (Douillet et al., 2013).** This hypothesis could be  
608 tested by applying our techniques to an appropriate selection of samples from a range of locations.

609

## 610 **6. Conclusions**

611 Three fragmentation methods (rapid decompression, impact and milling) have been explored to  
612 constrain fragmentation associated with three different eruptive processes (Figure 11). Analysed  
613 GSDs are fractal, which means that they can be characterised by the fractal dimension  $D$ . Our data  
614 show that an initial GSD with  $D \approx 2.1$  produced by rapid decompression can be altered by secondary  
615 fragmentation processes that generate fine particles. Importantly, however,  $D$  values produced by  
616 secondary processes in our experiments reach only  $\sim 2.7$  (Fig. 8), which is far from  $D > 3$  observed in  
617 many silicic eruptions (e.g., Kaminski and Jaupart, 1998; Rust and Cashman, 2011). We suggest that  
618 the relatively low  $D$  values reflect the role of the groundmass crystal population, which prevents  
619 extensive crushing and grain size reduction.

620

621 We support this hypothesis by analysis of particle shape (Fig. 4), componentry (Fig. 5) and adherence  
622 factor (AF; Fig. 9). These data show that secondary fragmentation by either impact or milling  
623 dramatically reduces the matrix component (Fig. 5b); ash generated by milling becomes increasingly  
624 rounded (less elongate), and ash exteriors generated by impacts becomes increasingly smooth (Fig. 4).  
625 Both milling and impact also remove adhering matrix from crystals (decrease AF), with milling the



626 most efficient at this process. Importantly, products of primary fragmentation retain much more  
627 adhering matrix than products of secondary fragmentation by either milling or impact (Fig. 9).  
628 Together these data provide guidelines for assessing primary vs. secondary contributions to the total  
629 grain size population within an eruptive deposit.

630

631 To further explore the role of crystals, we analysed the crystal content of volcanic ash derived from  
632 rapid decompression. Most crystals fracture along cleavage planes, leaving a smooth and clean  
633 breakage surface. During the evacuation of a crystal-rich magma body driven by rapid decompression,  
634 crystal fragmentation is inevitable and indeed characteristic of the associated tephra fallout. The  
635 proportion of free crystals depends on the grain size considered. X-Ray CT measurements combined  
636 with componentry allowed us to describe the shift in crystal size during fragmentation by rapid  
637 decompression. These data are important because the size fractions dominated by juvenile crystals  
638 show enhanced sedimentation because crystal densities exceed those of vesicular clasts. Thus we  
639 suggest that consideration of crystal sizes and proportions could improve settling calculations that  
640 inform hazard maps and dispersion models.

641

642 Finally we illustrate the application of our analysis techniques to two samples from Soufriere Hills  
643 Volcano, Montserrat: one dome collapse sample with co-PDC ash only, and one Vulcanian sample  
644 with contributions from both primary and co-PDC fragmentation. These samples are distinct in both  
645 their components and their grain characteristics, particularly AF. The Vulcanian sample is dominated  
646 by deep-derived microlite-poor and highly vesicular glass. Ash particles have polymodal AF  
647 distributions, with a dominant mode at low AF (little adhering glass) and two other modes at higher  
648 AF. We suggest that the high AF modes reflect primary fragmentation, while the low AF mode is the  
649 signature of co-PDC ash. The dome collapse sample, in contrast, is dominated by microlite-rich glass  
650 of variable vesicularity. In this sample, the AF distribution is approximately uniform, and most likely  
651 reflects the wide range of groundmass textures (both vesicularity and crystallinity). This latter  
652 observation brings up one further point, which is that both primary and secondary fragmentation  
653 processes are strongly dependent on the original magma components. As a result, a full understanding

654 of ash attributes produced by different mechanisms requires a systematic study using starting  
655 materials with different bubble and crystal attributes.

656

## 657 **Acknowledgements**

658 We thank the Henry Mosely X-Ray Imaging Facility, University of Manchester for their support with  
659 the XRCT. Klaus Mayer and Cristian Montanaro are thanked for their support with the shock tube  
660 experiments. KVC acknowledges the support of the AXA Research Fund and a Royal Society  
661 Research Merit Award. TJJ was partly supported by NERC studentship NE/L0025901.

662

663

## 664 **References:**

665

- 666 Alatorre-Ibargüengoitia, M. A., Scheu, B., Dingwell, D. B., Delgado-Granados, H., and Taddeucci, J.,  
667 2010, Energy consumption by magmatic fragmentation and pyroclast ejection during  
668 Vulcanian eruptions: Earth and Planetary Science Letters, v. 291, no. 1, p. 60-69.
- 669 Alfano, F., Bonadonna, C., Volentik, A. C., Connor, C. B., Watt, S. F., Pyle, D. M., and Connor, L. J.,  
670 2011, Tephra stratigraphy and eruptive volume of the May, 2008, Chaitén eruption, Chile:  
671 Bulletin of Volcanology, v. 73, no. 5, p. 613-630.
- 672 Alidibirov, M., and Dingwell, D. B., 2000, Three fragmentation mechanisms for highly viscous magma  
673 under rapid decompression: Journal of Volcanology and Geothermal Research, v. 100, no. 1–  
674 4, p. 413-421.
- 675 Bachmann, O., Dungan, M. A., and Lipman, P. W., 2002, The Fish Canyon magma body, San Juan  
676 volcanic field, Colorado: rejuvenation and eruption of an upper-crustal batholith: Journal of  
677 Petrology, v. 43, no. 8, p. 1469-1503.
- 678 Best, M. G., and Christiansen, E. H., 1997, Origin of broken phenocrysts in ash-flow tuffs: Geological  
679 Society of America Bulletin, v. 109, no. 1, p. 63-73.
- 680 Bindeman, I. N., 2005, Fragmentation phenomena in populations of magmatic crystals: American  
681 Mineralogist, v. 90, no. 11-12, p. 1801-1815.
- 682 Bonadonna, C., Connor, L. J., Connor, C. B., and Courtland, L. M., 2010, Tephra2.
- 683 Bonadonna, C., Mayberry, G., Calder, E., Sparks, R., Choux, C., Jackson, P., Lejeune, A., Loughlin, S.,  
684 Norton, G., and Rose, W., 2002, Tephra fallout in the eruption of Soufrière Hills Volcano,  
685 Montserrat: Geological Society, London, Memoirs, v. 21, no. 1, p. 483-516.
- 686 Borg, I. Y., and Heard, H. C., 1970, Experimental Deformation Of Plagioclases, *in* Paulitsch, P., ed.,  
687 Experimental and Natural Rock Deformation / Experimentelle und natürliche  
688 Gesteinsverformung, Springer Berlin Heidelberg, p. 375-403.
- 689 Brown, W. L., and Macaudière, J., 1984, Microfracturing in relation to atomic structure of plagioclase  
690 from a deformed meta-anorthosite: Journal of Structural Geology, v. 6, no. 5, p. 579-586.
- 691 Cagnoli, B., and Manga, M., 2004, Granular mass flows and Coulomb's friction in shear cell  
692 experiments: Implications for geophysical flows: Journal of Geophysical Research: Earth  
693 Surface (2003–2012), v. 109, no. F4.
- 694 Carter, N. L., Officer, C. B., Chesner, C. A., and Rose, W. I., 1986, Dynamic deformation of volcanic  
695 ejecta from the Toba caldera: Possible relevance to Cretaceous/Tertiary boundary  
696 phenomena: Geology, v. 14, no. 5, p. 380-383.

697 Chouet, B. A., Page, R. A., Stephens, C. D., Lahr, J. C., and Power, J. A., 1994, Precursory swarms of  
698 long-period events at Redoubt Volcano (1989–1990), Alaska: Their origin and use as a  
699 forecasting tool: *Journal of Volcanology and Geothermal Research*, v. 62, no. 1–4, p. 95-135.

700 Cnudde, V., Masschaele, B., Dierick, M., Vlassenbroeck, J., Hoorebeke, L. V., and Jacobs, P., 2006,  
701 Recent progress in X-ray CT as a geosciences tool: *Applied Geochemistry*, v. 21, no. 5, p. 826-  
702 832.

703 Cordonnier, B., Hess, K. U., Lavallee, Y., and Dingwell, D. B., 2009, Rheological properties of dome  
704 lavas: Case study of Unzen volcano: *Earth and Planetary Science Letters*, v. 279, no. 3–4, p.  
705 263-272.

706 Darteville, S., Ernst, G. G., Stix, J., and Bernard, A., 2002, Origin of the Mount Pinatubo climactic  
707 eruption cloud: Implications for volcanic hazards and atmospheric impacts: *Geology*, v. 30,  
708 no. 7, p. 663-666.

709 Douillet, G. A., Tsang-Hin-Sun, È., Kueppers, U., Letort, J., Pacheco, D. A., Goldstein, F., Von Aulock,  
710 F., Lavallée, Y., Hanson, J. B., and Bustillos, J., 2013, Sedimentology and geomorphology of  
711 the deposits from the August 2006 pyroclastic density currents at Tungurahua volcano,  
712 Ecuador: *Bulletin of Volcanology*, v. 75, no. 11, p. 1-21.

713 Dufek, J., and Manga, M., 2008, In situ production of ash in pyroclastic flows: *Journal of Geophysical*  
714 *Research: Solid Earth*, v. 113, no. B9.

715 Elangovan, P., Hezel, D. C., Howard, L., Armstrong, R., and Abel, R. L., 2012, PhaseQuant: A tool for  
716 quantifying tomographic data sets of geological specimens: *Computers & Geosciences*, v. 48,  
717 no. 0, p. 323-329.

718 Engwell, S., Sparks, R., and Carey, S., 2014, Physical characteristics of tephra layers in the deep sea  
719 realm: the Campanian Ignimbrite eruption: *Geological Society, London, Special Publications*,  
720 v. 398, no. 1, p. 47-64.

721 **Engwell, S., Eychenne, J., 2016. Chapter 4: Contribution of fine ash to the atmosphere from**  
722 **plumes associated with pyroclastic density currents. In *Volcanic Ash: Hazard Observation*, edited**  
723 **by Mackie, S., Ricketts, H., Watson, M., Cashman, K., Rust, A. Elsevier. 67-85pp.**

724 Eychenne, J., Cashman, K., Rust, A., and Durant, A., 2015, Impact of the lateral blast on the spatial  
725 pattern and grain size characteristics of the 18 May 1980 Mount St. Helens fallout deposit:  
726 *Journal of Geophysical Research: Solid Earth*, v. 120, no. 9, p. 6018-6038.

727 Eychenne, J., Le Penneç, J.-L., Troncoso, L., Gouhier, M., and Nedelec, J.-M., 2012, Causes and  
728 consequences of bimodal grain-size distribution of tephra fall deposited during the August  
729 2006 Tungurahua eruption (Ecuador): *Bulletin of volcanology*, v. 74, no. 1, p. 187-205.

730 Félix, G., and Thomas, N., 2004, Relation between dry granular flow regimes and morphology of  
731 deposits: formation of levées in pyroclastic deposits: *Earth and Planetary Science Letters*, v.  
732 221, no. 1, p. 197-213.

733 Freundt, A., and Schmincke, H.-U., 1992, Abrasion in pyroclastic flows: *Geologische Rundschau*, v. 81,  
734 no. 2, p. 383-389.

735 Genareau, K., Proussevitch, A. A., Durant, A. J., Mulukutla, G., and Sahagian, D. L., 2012, Sizing up the  
736 bubbles that produce very fine ash during explosive volcanic eruptions: *Geophysical*  
737 *Research Letters*, v. 39, no. 15.

738 Hartmann, W. K., 1969, Terrestrial, lunar, and interplanetary rock fragmentation: *Icarus*, v. 10, no. 2,  
739 p. 201-213.

740 Hull, D., 1999, *Fractography: observing, measuring and interpreting fracture surface topography*,  
741 Cambridge University Press.

742 Jones, T., Wadsworth, F., Vasseur, J., Lavallee, Y., Hess, K., Scheu, B., and Dingwell, D., Porosity and  
743 Textural Evolution of Bubbly Magma under High-Temperature Uniaxial Deformation, *in*  
744 *Proceedings AGU Fall Meeting Abstracts2013, Volume 1*, p. 2715.

745 Kaminski, E., and Jaupart, C., 1998, The size distribution of pyroclasts and the fragmentation  
746 sequence in explosive volcanic eruptions: *Journal of Geophysical Research: Solid Earth*, v.  
747 103, no. B12, p. 29759-29779.

748 Kelly, A., and Macmillan, N. H., 1986, Strong solids, Clarendon Press Oxford.

749 Kennedy, B., Spieler, O., Scheu, B., Kueppers, U., Taddeucci, J., and Dingwell, D. B., 2005, Conduit  
750 implosion during Vulcanian eruptions: *Geology*, v. 33, no. 7, p. 581-584.

751 Korvin, G., 1992, Fractal models in the earth sciences, Elsevier Science Ltd.

752 Kueppers, U., Perugini, D., and Dingwell, D. B., 2006a, "Explosive energy" during volcanic eruptions  
753 from fractal analysis of pyroclasts: *Earth and Planetary Science Letters*, v. 248, no. 3, p. 800-  
754 807.

755 Kueppers, U., Putz, C., Spieler, O., and Dingwell, D. B., 2012, Abrasion in pyroclastic density currents:  
756 insights from tumbling experiments: *Physics and Chemistry of the Earth, Parts A/B/C*, v. 45,  
757 p. 33-39.

758 Kueppers, U., Scheu, B., Spieler, O., and Dingwell, D. B., 2006b, Fragmentation efficiency of explosive  
759 volcanic eruptions: a study of experimentally generated pyroclasts: *Journal of Volcanology  
760 and Geothermal Research*, v. 153, no. 1, p. 125-135.

761 Liu, E., Cashman, K., Rust, A., and Gislason, S., 2015a, The role of bubbles in generating fine ash  
762 during hydromagmatic eruptions: *Geology*, v. 43, no. 3, p. 239-242.

763 Liu, E. J., Cashman, K. V., and Rust, A. C., 2015b, Optimising shape analysis to quantify volcanic ash  
764 morphology: *GeoResJ*, v. 8, p. 14-30.

765 Manga, M., Patel, A., and Dufek, J., 2011, Rounding of pumice clasts during transport: field  
766 measurements and laboratory studies: *Bulletin of Volcanology*, v. 73, no. 3, p. 321-333.

767 Martel, C., Dingwell, D. B., Spieler, O., Pichavant, M., and Wilke, M., 2001, Experimental  
768 fragmentation of crystal-and vesicle-bearing silicic melts: *Bulletin of volcanology*, v. 63, no. 6,  
769 p. 398-405.

770 Meyer, J., 1971, Glass crust on intratelluric phenocrysts in volcanic ash as a measure of eruptive  
771 violence: *Bulletin Volcanologique*, v. 35, no. 2, p. 358-368.

772 Miwa, T., and Geshi, N., 2012, Decompression rate of magma at fragmentation: Inference from  
773 broken crystals in pumice of vulcanian eruption: *Journal of Volcanology and Geothermal  
774 Research*, v. 227, p. 76-84.

775 Mueller, S. B., Lane, S. J., and Kueppers, U., 2015, Lab-scale ash production by abrasion and collision  
776 experiments of porous volcanic samples: *Journal of Volcanology and Geothermal Research*,  
777 v. 302, p. 163-172.

778 Pallister, J. S., Hoblitt, R. P., Meeker, G. P., Knight, R. J., and Siems, D. F., 1996, Magma mixing at  
779 Mount Pinatubo: petrographic and chemical evidence from the 1991 deposits: *Fire and Mud:  
780 Eruptions and Lahars of Mount Pinatubo, Philippines*. Quezon City: Philippine Institute of  
781 Volcanology and Seismology, p. 687-731.

782 Perugini, D., and Kueppers, U., 2012, Fractal analysis of experimentally generated pyroclasts: A tool  
783 for volcanic hazard assessment: *Acta Geophysica*, v. 60, no. 3, p. 682-698.

784 Perugini, D., Speziali, A., Caricchi, L., and Kueppers, U., 2011, Application of fractal fragmentation  
785 theory to natural pyroclastic deposits: Insights into volcanic explosivity of the Valentano  
786 scoria cone (Italy): *Journal of Volcanology and Geothermal Research*, v. 202, no. 3, p. 200-  
787 210.

788 Rose, W., and Durant, A., 2009, Fine ash content of explosive eruptions: *Journal of Volcanology and  
789 Geothermal Research*, v. 186, no. 1, p. 32-39.

790 Rust, A., and Cashman, K., 2011, Permeability controls on expansion and size distributions of  
791 pyroclasts: *Journal of Geophysical Research: Solid Earth*, v. 116, no. B11.

792 Scheu, B., Kueppers, U., Mueller, S., Spieler, O., and Dingwell, D. B., 2008, Experimental volcanology  
793 on eruptive products of Unzen volcano: *Journal of Volcanology and Geothermal Research*, v.  
794 175, no. 1-2, p. 110-119.

795 Sparks, R., and Walker, G., 1977, The significance of vitric-enriched air-fall ashes associated with  
796 crystal-enriched ignimbrites: *Journal of Volcanology and Geothermal Research*, v. 2, no. 4, p.  
797 329-341.

- 798 Spieler, O., Kennedy, B., Kueppers, U., Dingwell, D. B., Scheu, B., and Taddeucci, J., 2004, The  
799 fragmentation threshold of pyroclastic rocks: *Earth and Planetary Science Letters*, v. 226, no.  
800 1–2, p. 139-148.
- 801 Taddeucci, J., Pompilio, M., and Scarlato, P., 2004, Conduit processes during the July–August 2001  
802 explosive activity of Mt. Etna (Italy): inferences from glass chemistry and crystal size  
803 distribution of ash particles: *Journal of Volcanology and Geothermal Research*, v. 137, no. 1,  
804 p. 33-54.
- 805 Tait, S., 1992, Selective preservation of melt inclusions in igneous phenocrysts: *American*  
806 *Mineralogist*, v. 77, no. 1-2, p. 146-155.
- 807 Turcotte, D., 1986, Fractals and fragmentation: *Journal of Geophysical Research: Solid Earth (1978–*  
808 *2012)*, v. 91, no. B2, p. 1921-1926.
- 809 Walker, G. P., 1973, Explosive volcanic eruptions—a new classification scheme: *Geologische*  
810 *Rundschau*, v. 62, no. 2, p. 431-446.
- 811 Williamson, B., Di Muro, A., Horwell, C., Spieler, O., and Llewelin, E., 2010, Injection of vesicular  
812 magma into an andesitic dome at the effusive–explosive transition: *Earth and Planetary*  
813 *Science Letters*, v. 295, no. 1, p. 83-90.
- 814 Zhang, Y., 1998, Mechanical and phase equilibria in inclusion-host systems: *Earth and Planetary*  
815 *Science Letters*, v. 157, no. 3-4, p. 209-222.
- 816 Zimanowski, B., Wohletz, K., Dellino, P., and Büttner, R., 2003, The volcanic ash problem: *Journal of*  
817 *Volcanology and Geothermal Research*, v. 122, no. 1, p. 1-5.

818

819  
820  
821  
822  
823  
824  
825  
826  
827  
828  
829  
830  
831  
832  
833  
834  
835  
836  
837  
838  
839  
840  
841  
842  
843  
844  
845  
846

**Figure Captions:**

**Figure 1:** 3D surface reconstructions of the crystal phases. Processed using Avizo software from X-Ray computed tomography generated image stacks. **(a)** SHV subvolume. **(b)** Cumulative frequency diagram showing the relative crystal volume distributions within SHV pumice extracted from 3D reconstructions.

**Figure 2:** Diagrams of the various fragmentation apparatus used in this study. **(a)** shock tube (modified after Alatorre-Ibargüengoitia et al. (2010)), **(b)** falling piston and **(c)** ball mill.

**Figure 3:** Grain size distributions for **(a)** rapid decompression shock tube, **(b)** falling piston and **(c)** ball mill experiments.

**Figure 4:** Shape analysis from BSE SEM images of 2 $\phi$  grain size fraction. Histograms show shape data gathered from 2D SEM image mosaics. Where an axial ratio of one implies a perfectly round grain and a convexity of one implies a smooth grain with the same perimeter as its convex hull. **(a)** The difference in axial ratio of the grains produced by hot and cold decompression. **(b)** The change in the axial ratio value for grains that were hit 5 and 10 times. **(c)** The change in the axial ratio value for grains that were milled for 30 seconds and one minute. **(d)** The difference in convexity values of the grains produced by hot and cold decompression. **(e)** The change in value of convexity in grains hit 5 and 10 times. **(f)** The change in the value of convexity for grains that were milled for 30 seconds and one minute.

**Figure 5:** Componentry results for experimentally generated ash. **(a)** SHV average componentry results from rapid decompression, normalised per grain size fraction. **(b)** Individual ash grain componentry from the 2 $\phi$  grain size fraction using BSE SEM images of products of varying fragmentation techniques.

847 **Figure 6:** Normalised crystal distributions for SHV represented as a cumulative distribution. Solid  
848 lines represent the crystal population present in the volcanic core prior to experimental fragmentation.  
849 Dashed lines represent the experimentally fragmented crystal population.

850

851 **Figure 7:** SEM micrographs of crystals from the SHV 2 $\phi$  ash fraction. **(a)** Hornblende crystal  
852 showing mainly a clean flat surface however extremely irregular at the edges. **(b)** Broken crystal with  
853 a thin vesicular glass coating. **(c)** Hornblende crystal with a stepped fracture surface. **(d)** A plagioclase  
854 crystal showing multiple river line fractures on broken crystal surface.

855

856 **Figure 8:** Power law plots for **(a)** the rapid decompression experiments, **(b)** the falling piston  
857 experiments and **(c)** the ball mill experiments. Data markers represent those included in the linear  
858 regression.

859

860 **Figure 9:** Adherence Factor plot of the three fragmentation techniques: Milling (0.5 minutes and 1  
861 minute), Impact (5 hits and 10 hits) rapid decompression (cold and hot) and natural samples  
862 (Vulcanian and dome collapse). Adherence Factor (AF) = area of matrix / (area of matrix + area of  
863 crystal) against the total cumulative per cent. A high value for AF represents a higher proportion of  
864 adhered matrix and thus the upper curve shows a greater amount of ‘matrix stripping’ than the lower  
865 curve. Normalised Grain No. is the value of AF in descending order, normalised to one.

866

867 **Figure 10:** Componentry of two natural SHV samples. The samples are from fallout deposits  
868 produced by a dome collapse event (on 31 March 1997) and a Vulcanian eruption (on 26 September  
869 1997) of Soufriere Hills Volcano.

870

871 **Figure 11:** A summary cartoon relating the three experimental fragmentation mechanism to the  
872 natural volcanic scenario. Primary fragmentation through rapid decompression produces pyroclasts

873 with  $D \sim 2.2$ . Then through abrasion and milling, selective secondary fragmentation increases  $D$  and  
874 adds to the fine ash component to the GSD.

875

876 **Table 1:** Summary of all experimental runs and characterisation. Grey fields indicate that the  
877 characterisation has been performed.

878

879 **Table 2:** A review of relevant fragmented material and the associated fractal dimensions obtained.

880

881 **Figure S1:** Individual power-law plots for each experimental fragmentation experiment: (a) rapid  
882 decompression (b) impact and (c) milling. Open circles represent the data points not included in the  
883 linear fitting.

884

885 **Figure S2:** Histogram of adherence factor values for decompression (hot and cold), impact (5 hits and  
886 10 hits), milling (30 seconds and 1 minute) and natural samples (Vulcanian and dome collapse).  
887 Shown on bars is the proportion of broken crystals amongst the crystal population where a broken  
888 crystal is defined as a crystal that clearly does not display an intact ring of zoning.

889

890



Table 1

[Click here to download Table: Table\\_1\\_exp\\_conditions.docx](#)

Fragmentation Mechanism	Experimental conditions	Pre-fragmentation characterisation					Post-fragmentation characterisation						
		Representative thin section	Representative XRCT scan	Connected porosity (%)	Isolated porosity (%)	Total porosity (%)	GSD	Fractals	Course Componentry	Fine (Ash) Componentry	Shape Analysis	Crystal volume shift	SEM imagery of fractures
Rapid Decompression	20°C, 15MPa			64.62	1.52	66.14							
	20°C, 30MPa			65.31	1.72	67.03							
	880°C, 15MPa			63.60	2.18	65.78							
	880°C, 30MPa			64.15	1.74	65.89							
Impact	5 Hits												
	10 Hits												
	15 Hits												
	20 Hits												
	25 Hits												
Milling	0.5 min												
	1 min												
	2.5 mins												
	5 mins												

Table 1: Jones et al (2016, JVGR)

Table 2

[Click here to download Table: Table\\_2\\_fractal\\_review.docx](#)

Material	Natural (N)/ Experimental (E)	D	Reference:
Mt Unzen 1992-95, 7% $\phi_c$	E	2.1	(Kueppers et al., 2006)
Mt Unzen 1992-95, 20.5% $\phi_c$	E	2.3	(Kueppers et al., 2006)
Mt Unzen 1992-95, 35.5% $\phi_c$	E	2.5	(Kueppers et al., 2006)
SHV (Rapid Decompression)	E	2.1*	This study
SHV (Impact)	E	2.6*	This study
SHV (Milling)	E	2.4*	This study
Falling Piston	E	2.6	(Kaminski and Jaupart, 1998)
Ball milling (without balls)	E	4.2	(Kaminski and Jaupart, 1998)
Ball milling (with balls)	E	5.4	(Kaminski and Jaupart, 1998)
Mt. Spurr August 1992	N (Total GSD)	3.0	(Durant and Rose, 2009)
Askja D, Iceland 1875	N (Fall)	3.0	(Sparks et al., 1981)
MSH, May 18, 1980 Plinian	N (Total GSD)	3.2	(Carey and Sigurdsson, 1982)
Mt. Spurr September 1992	N (Total GSD)	3.2	(Durant and Rose, 2009)
Hudson, Chile	N (Fall)	3.3	(Scasso et al., 1994)
Fogo A, Azores	N (Fall)	3.3	(Bursik et al., 1992)
Hachinohe, Japan	N (Fall)	3.5	(Hayakawa, 1985)
Krakatau, Indonesia	N (PDC)	3.3	(Carey et al., 1996)
Taupo, New Zealand	N (PDC)	3.3	(Walker and Wilson, 1983)
Fuego	N (Fall)	2.1	(Rust and Cashman, 2011)
Quizapu	N (Total GSD)	3.2	(Rust and Cashman, 2011)
Heimaey	N (Fall)	2.1	(Rust and Cashman, 2011)
El Chichon 1 and 3	N (Total GSD)	3.1	(Rust and Cashman, 2011)

\* Mean average D for that fragmentation mechanism. D reported to 1 d.p.

**Table 2:** Jones et al (2016, JVGR)

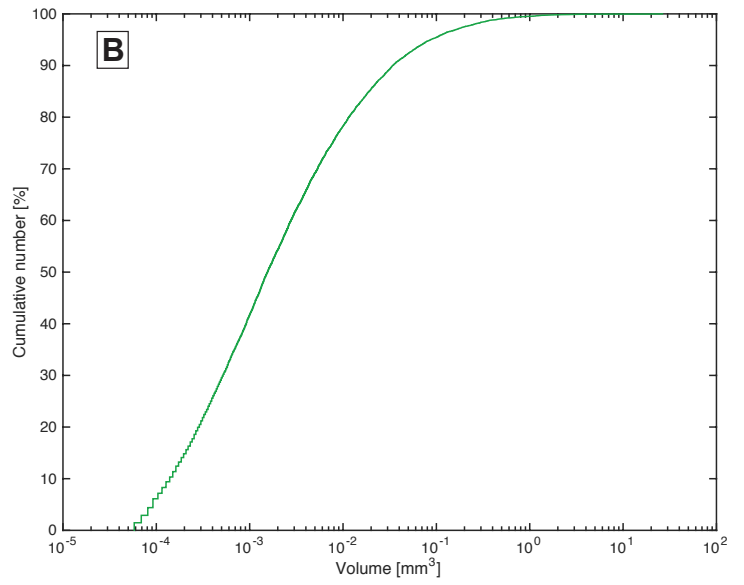
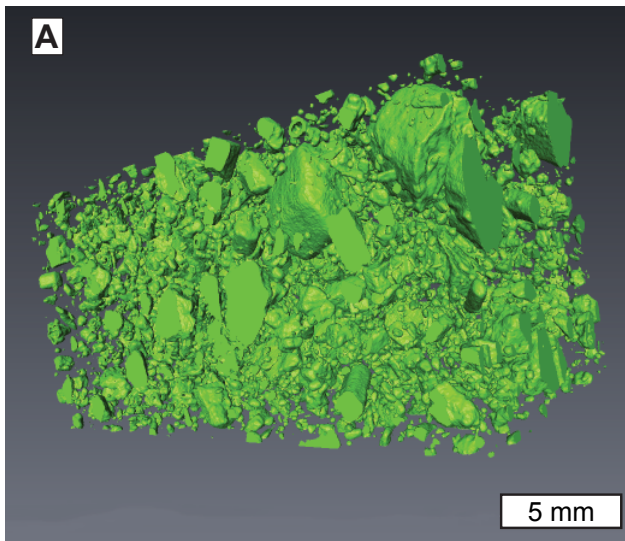
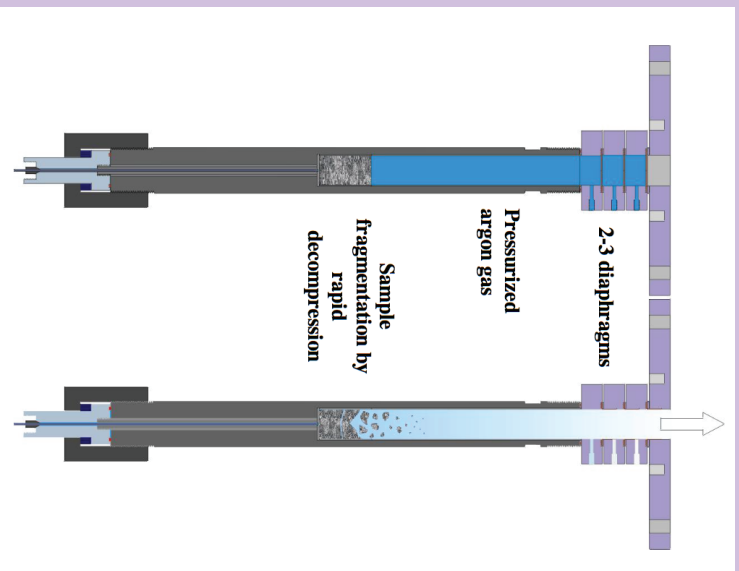
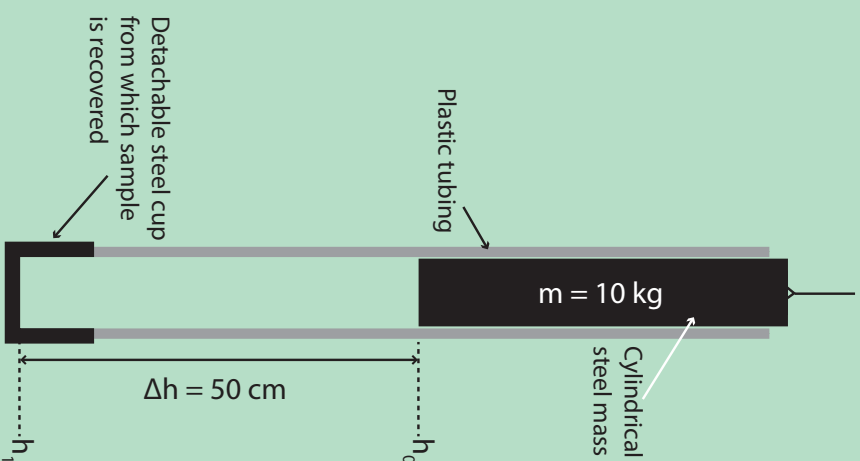


Figure 1: Jones et al (2016, JVGR)  
Size: 1.5 column

**A** Rapid Decompression (Shock Tube)



**B** Impact (Falling Piston)



**C** Milling (Planetary Ball Mill)

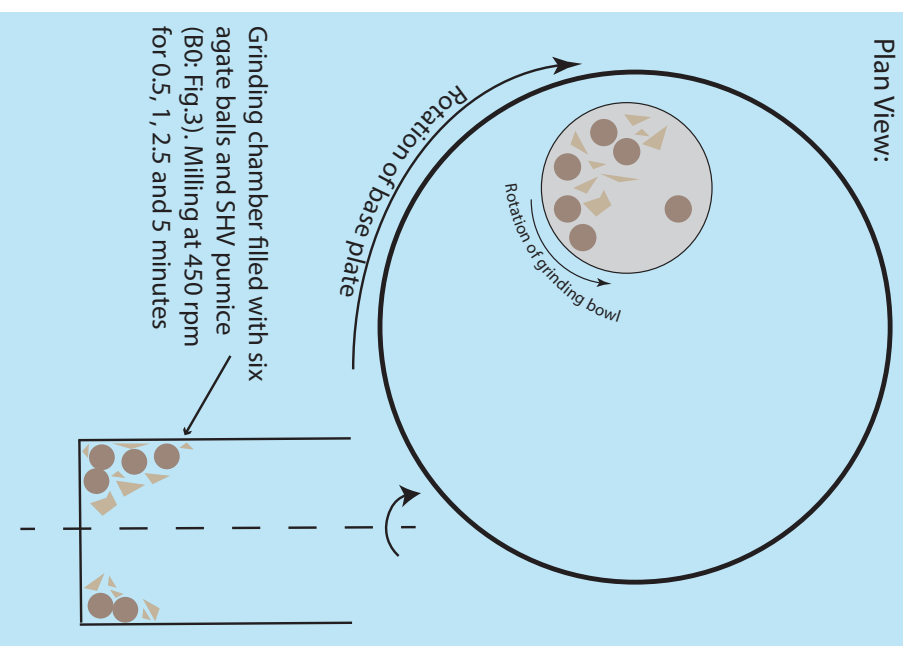


Figure 2: Jones et al. (2016, JVGR)  
Size: Double column

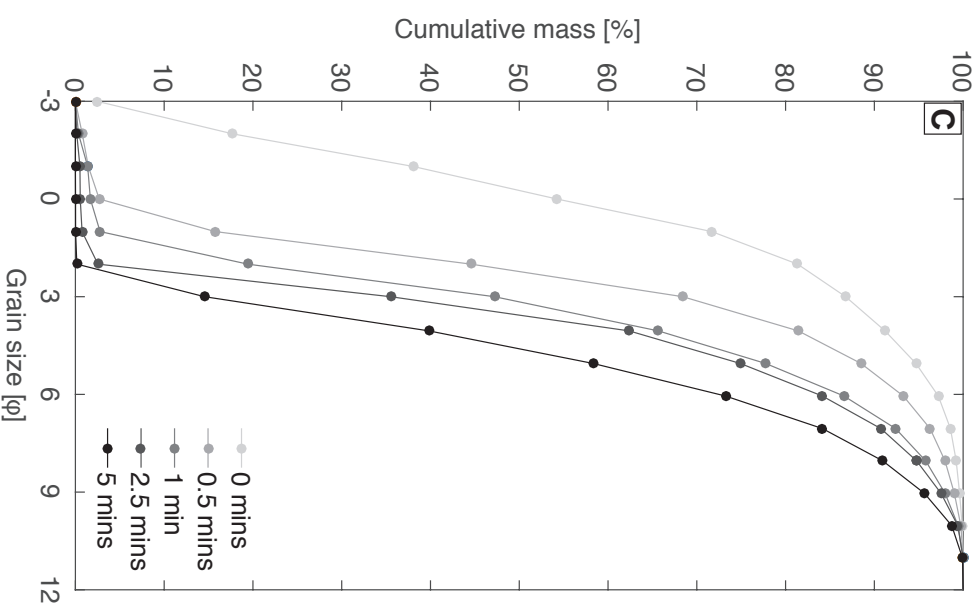
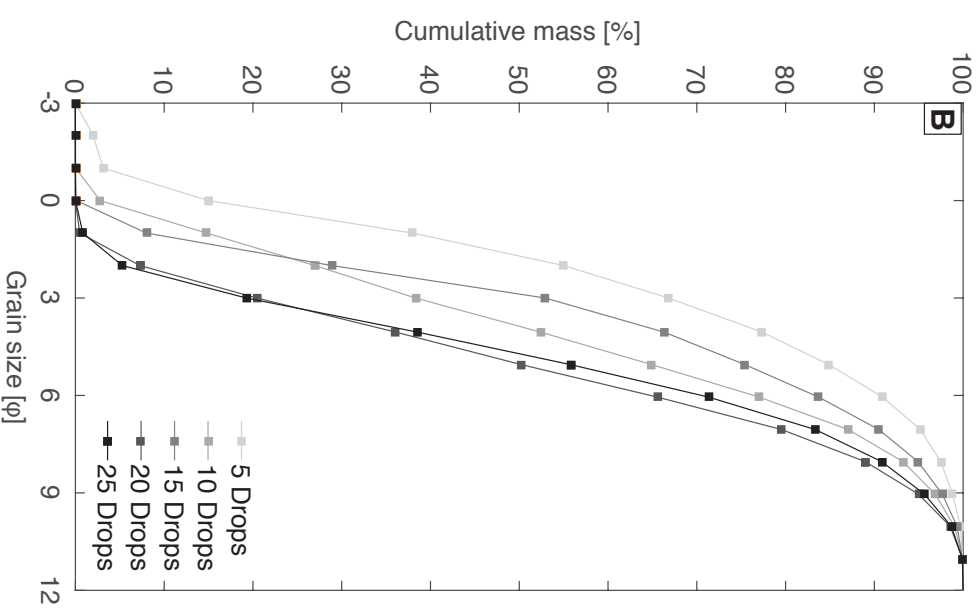
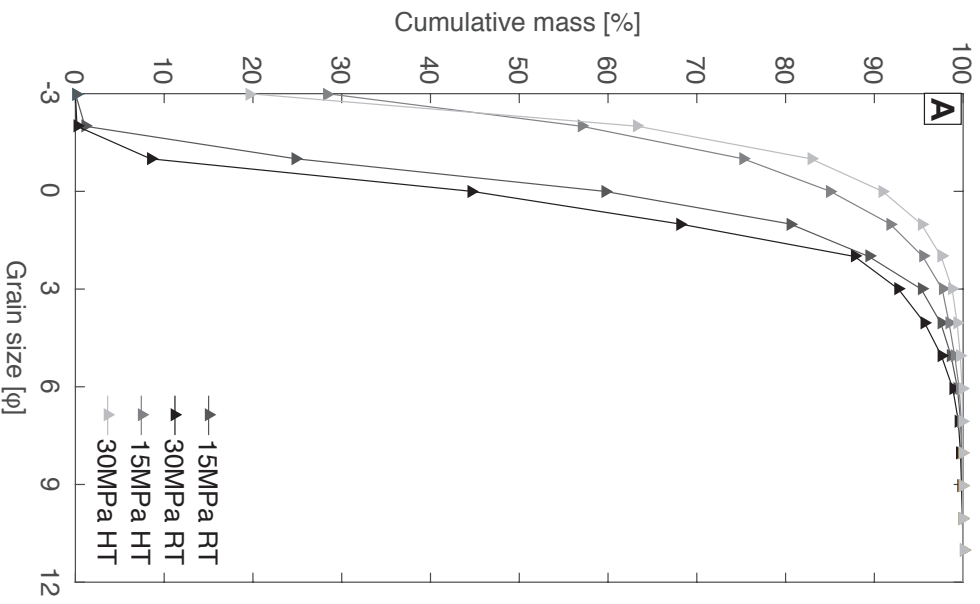


Figure 3: Jones et al. (2016, JVGR)  
 Size: Double column

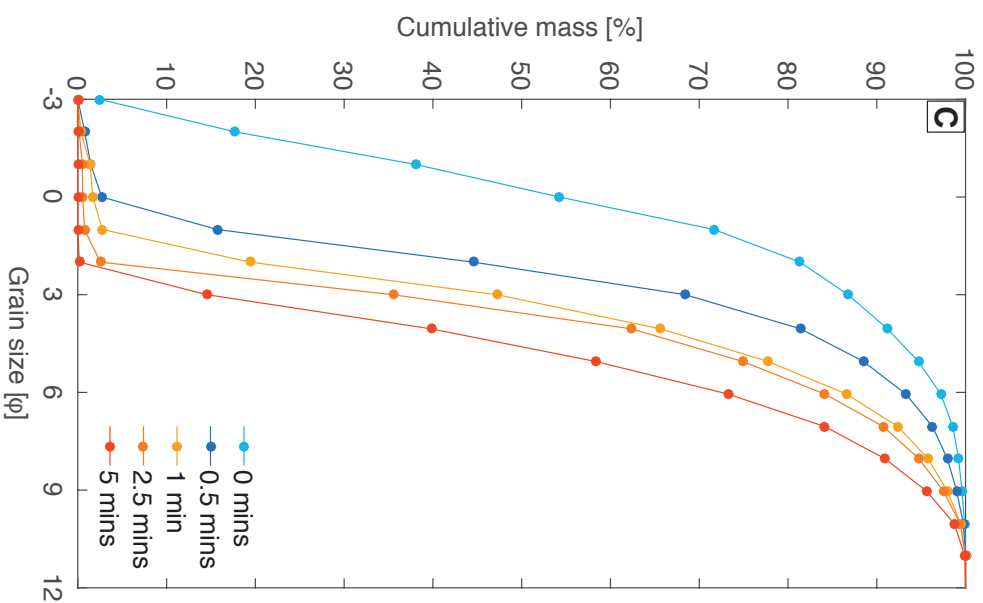
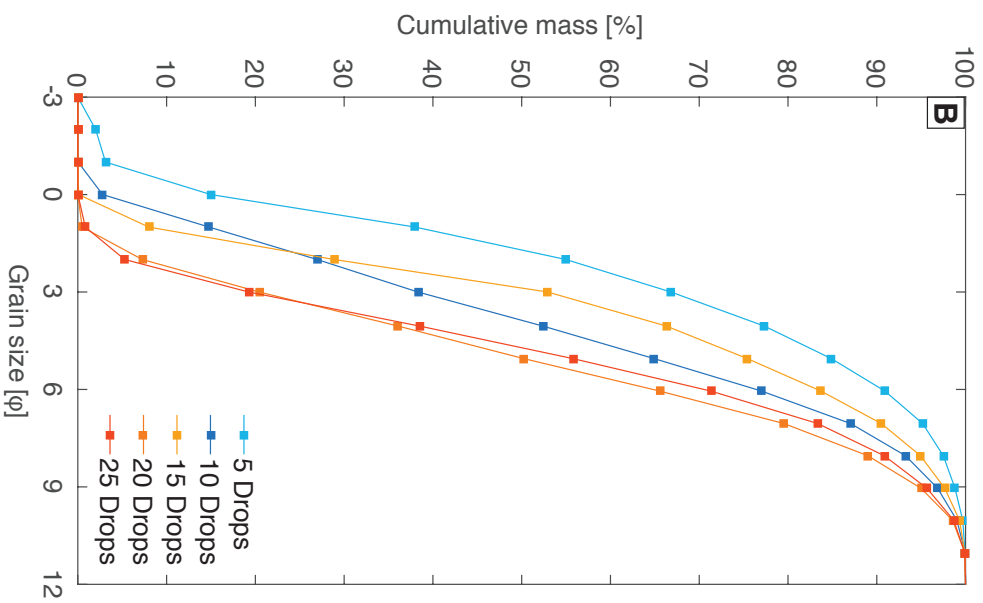
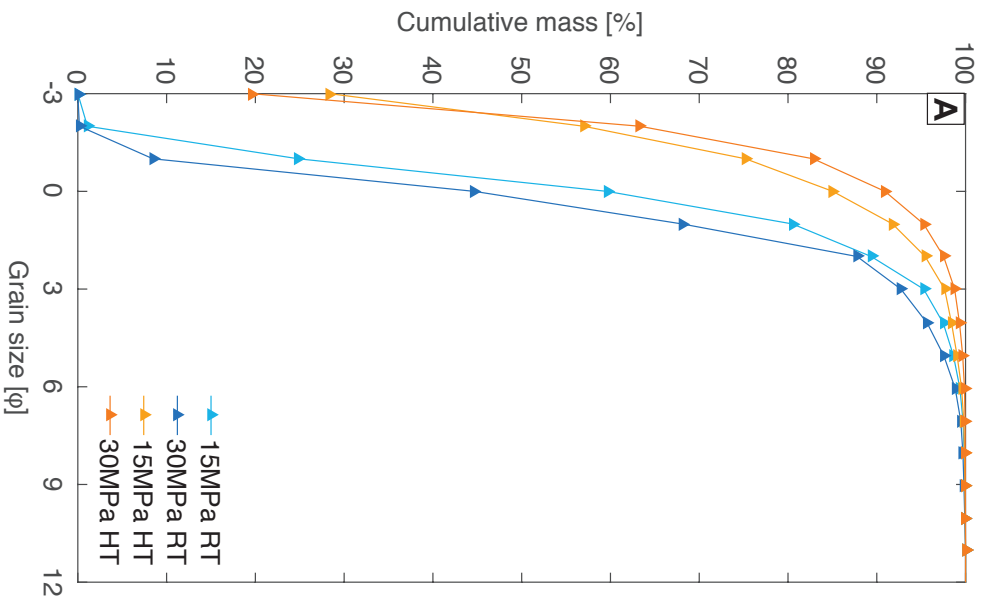


Figure 3: Jones et al. (2016, JVGR)  
Size: Double column

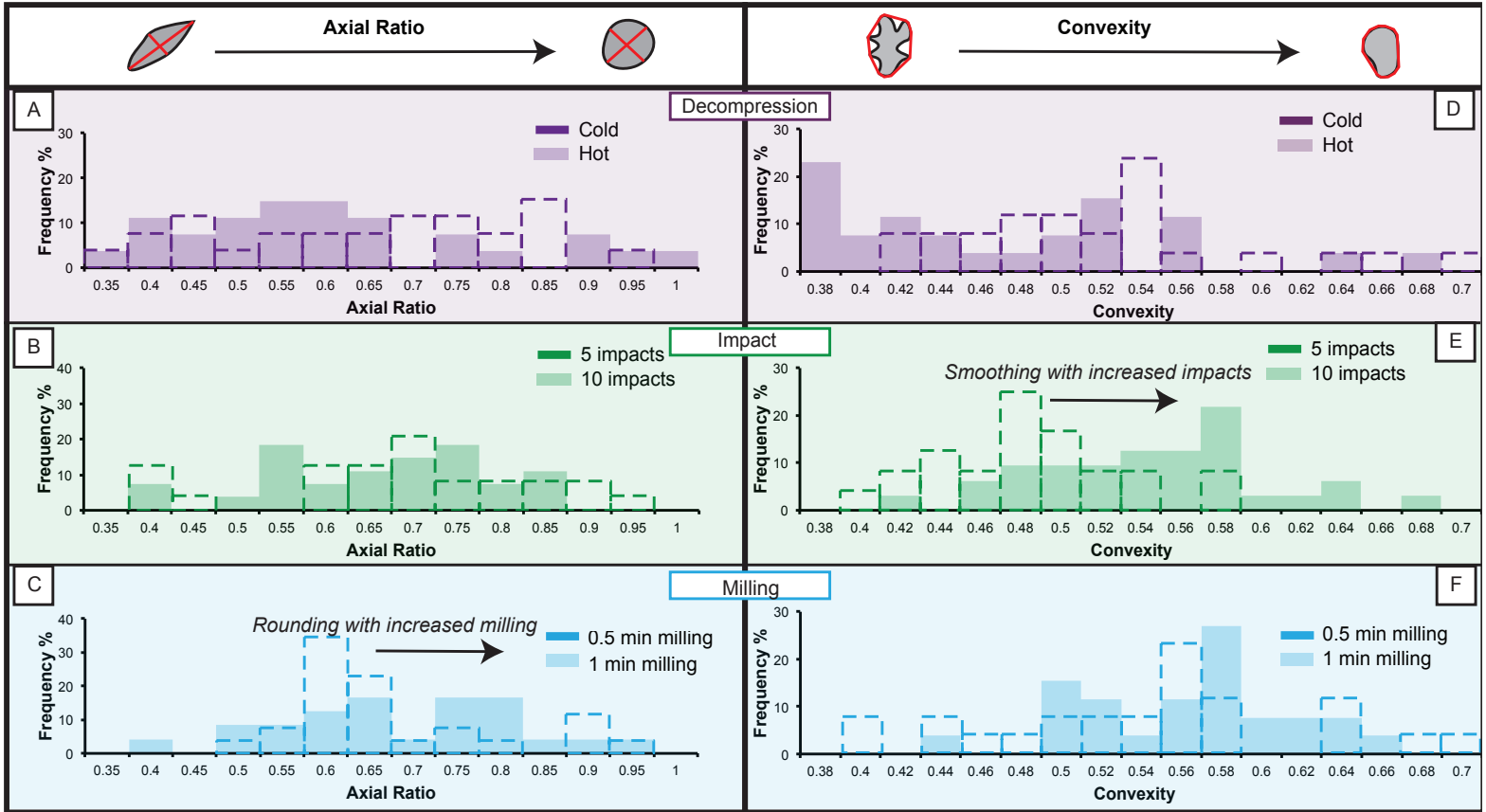


Figure 4: Jones et al. (2016, JGVR)  
Size: 2 column

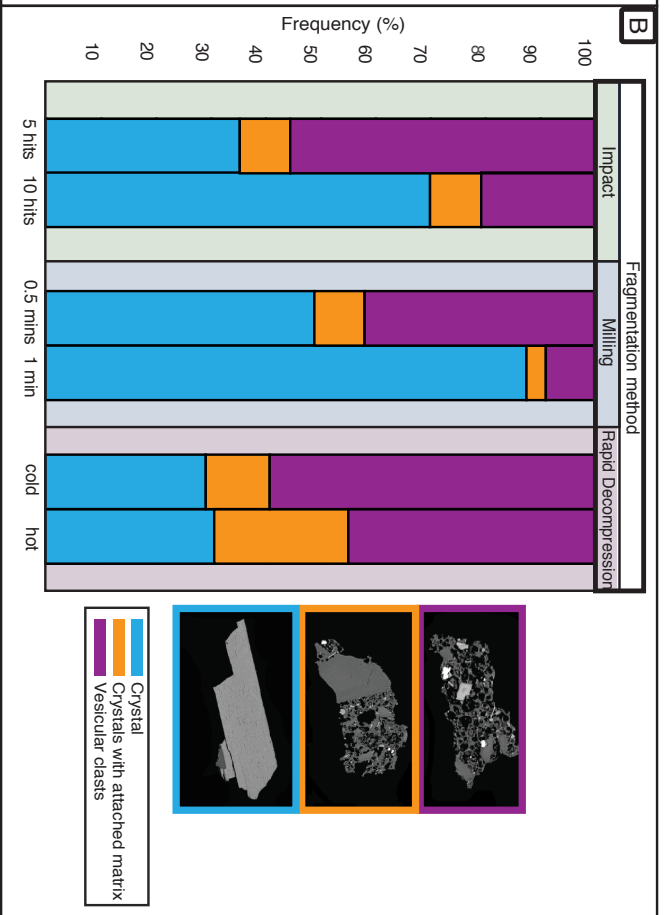
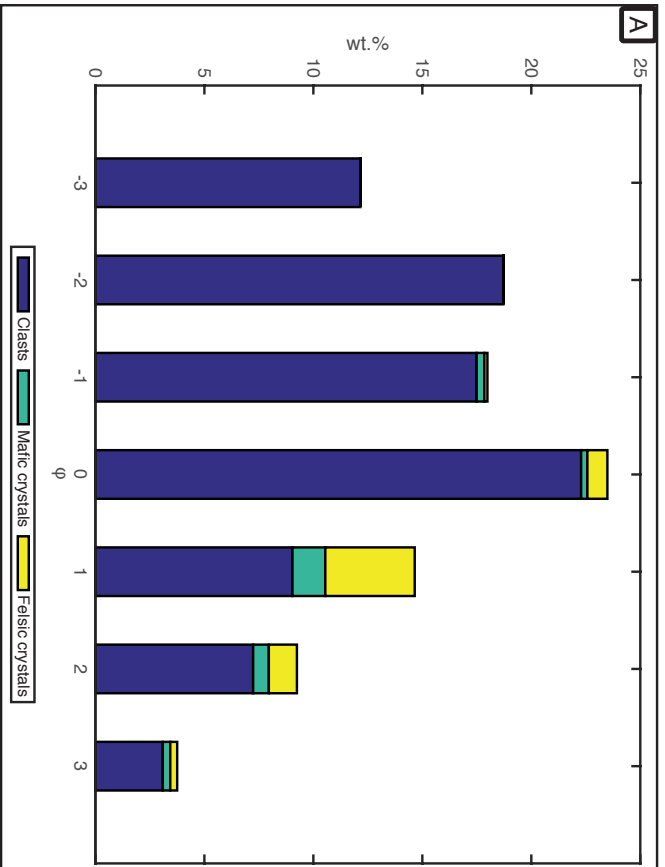


Figure 5: Jones et al (2016, JVGR)  
Size: Double Column



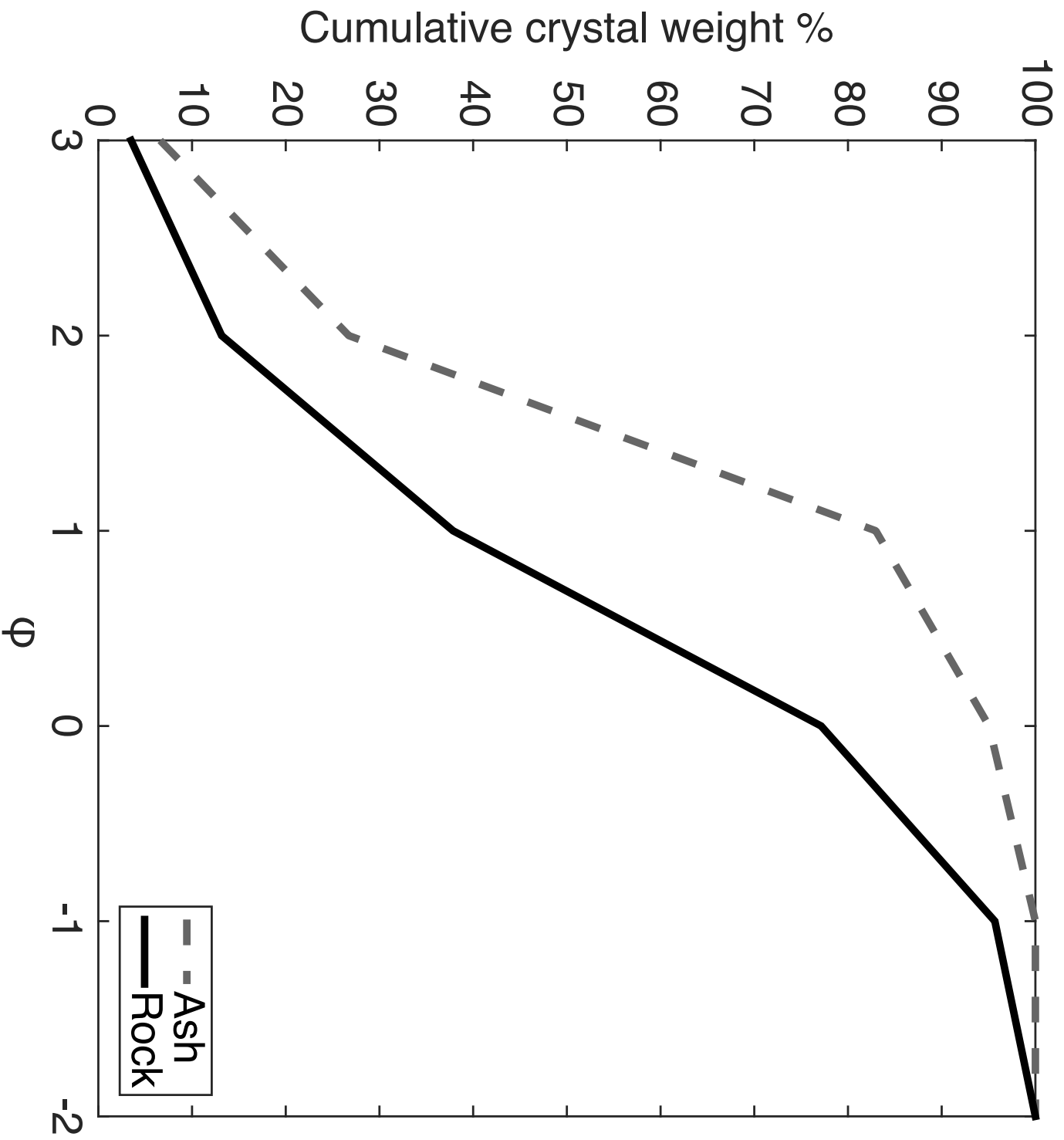


Figure 6: Jones et al. (2016, JVGR) Size: Single Column

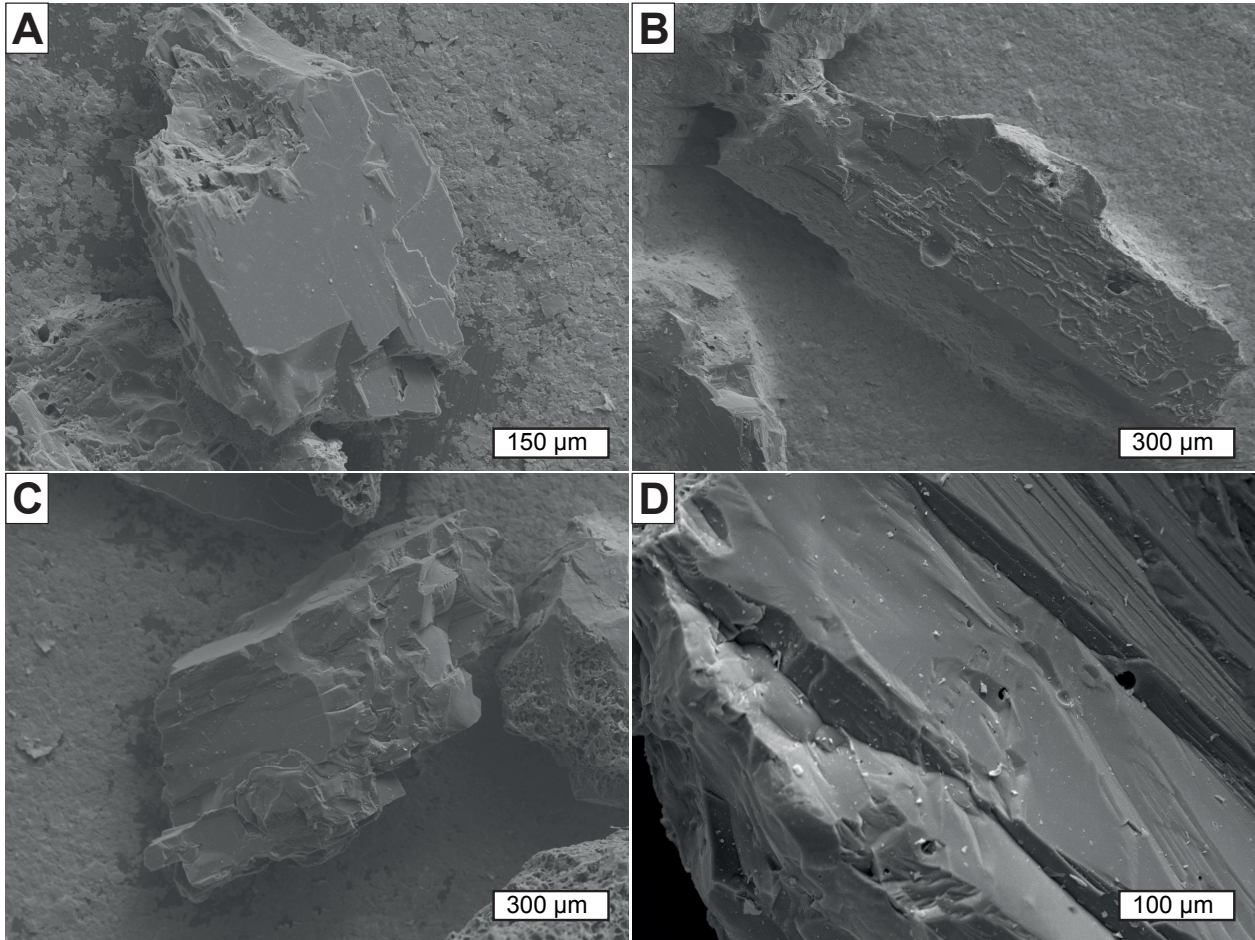


Figure 7: Jones et al (2016, JVGR)  
Size: Single column

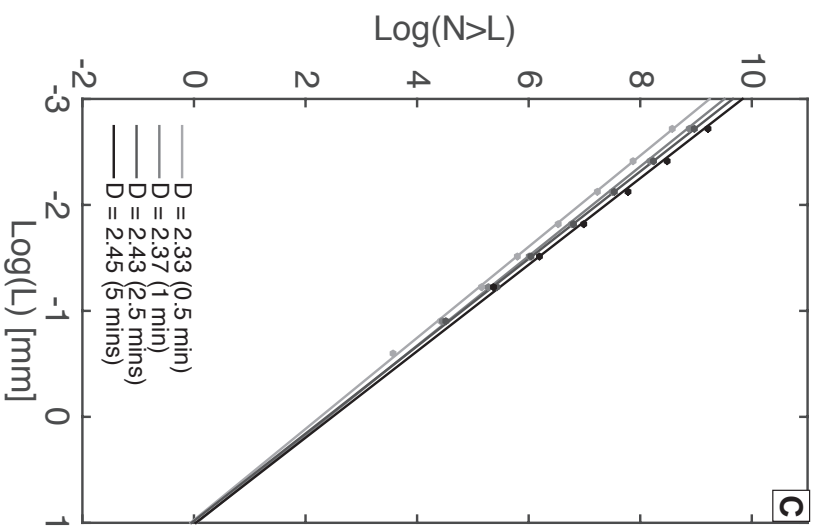
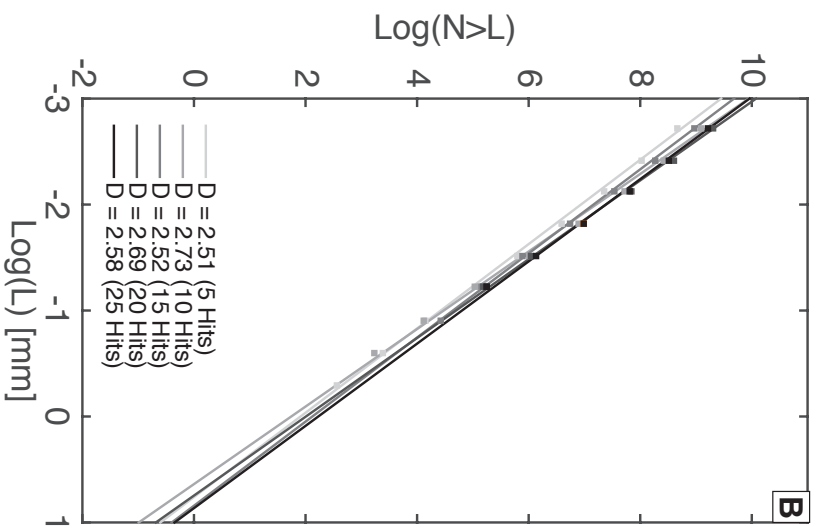
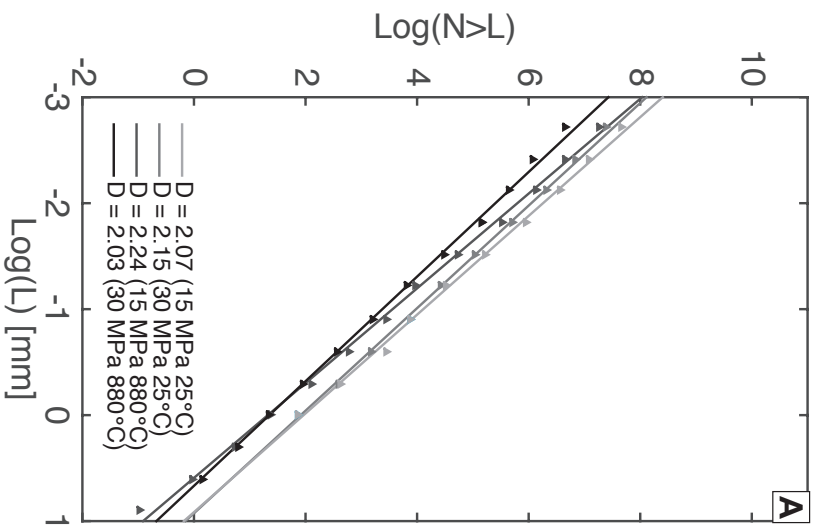


Figure 8: Jones et al. (2016, JVGR)  
 Size: Double column

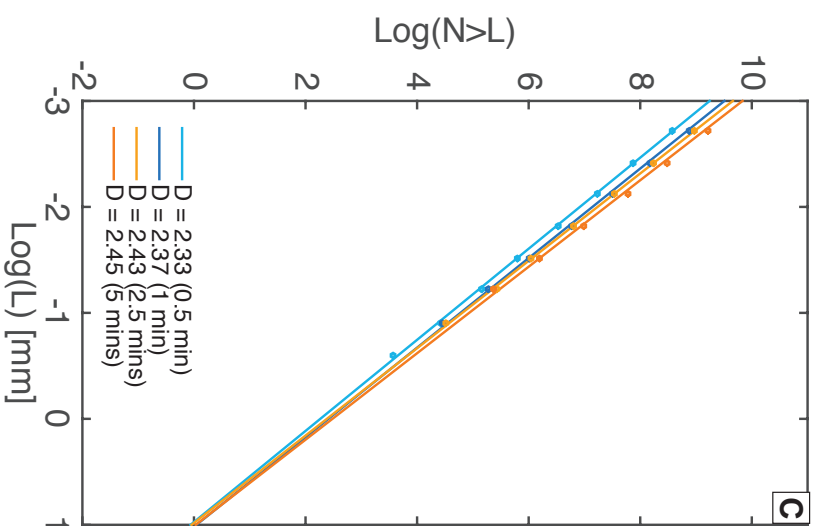
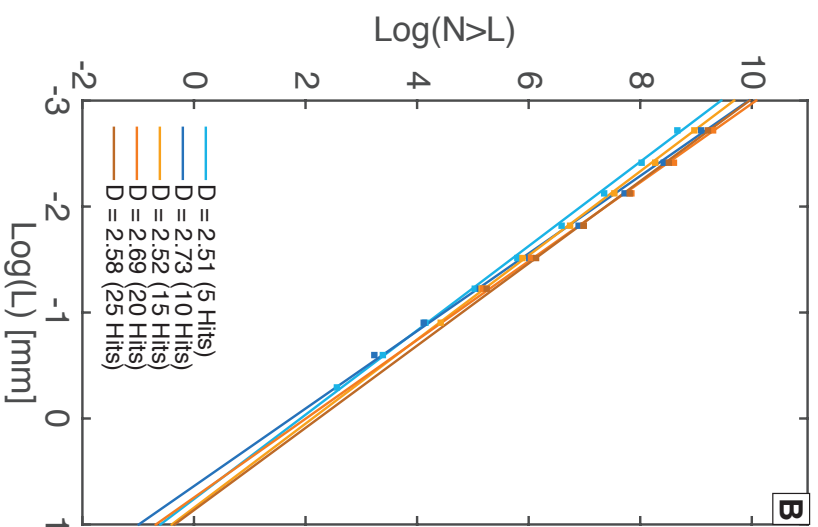
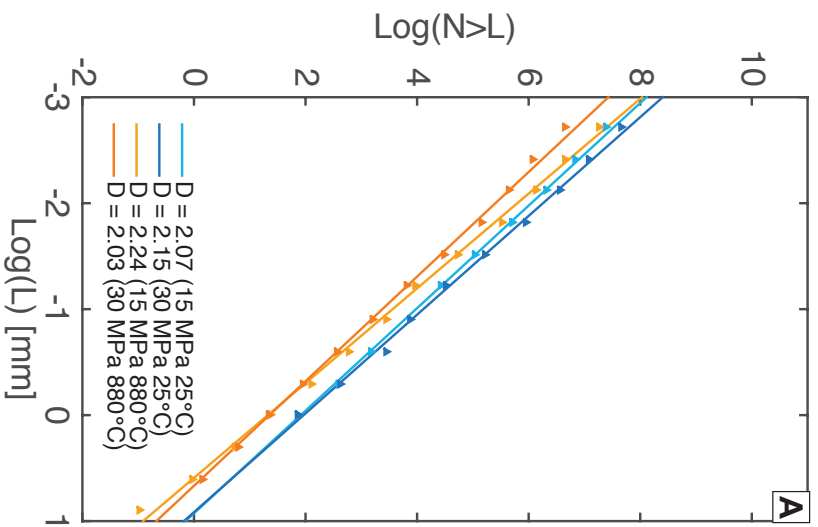


Figure 8: Jones et al. (2016, JVGR)  
Size: Double column

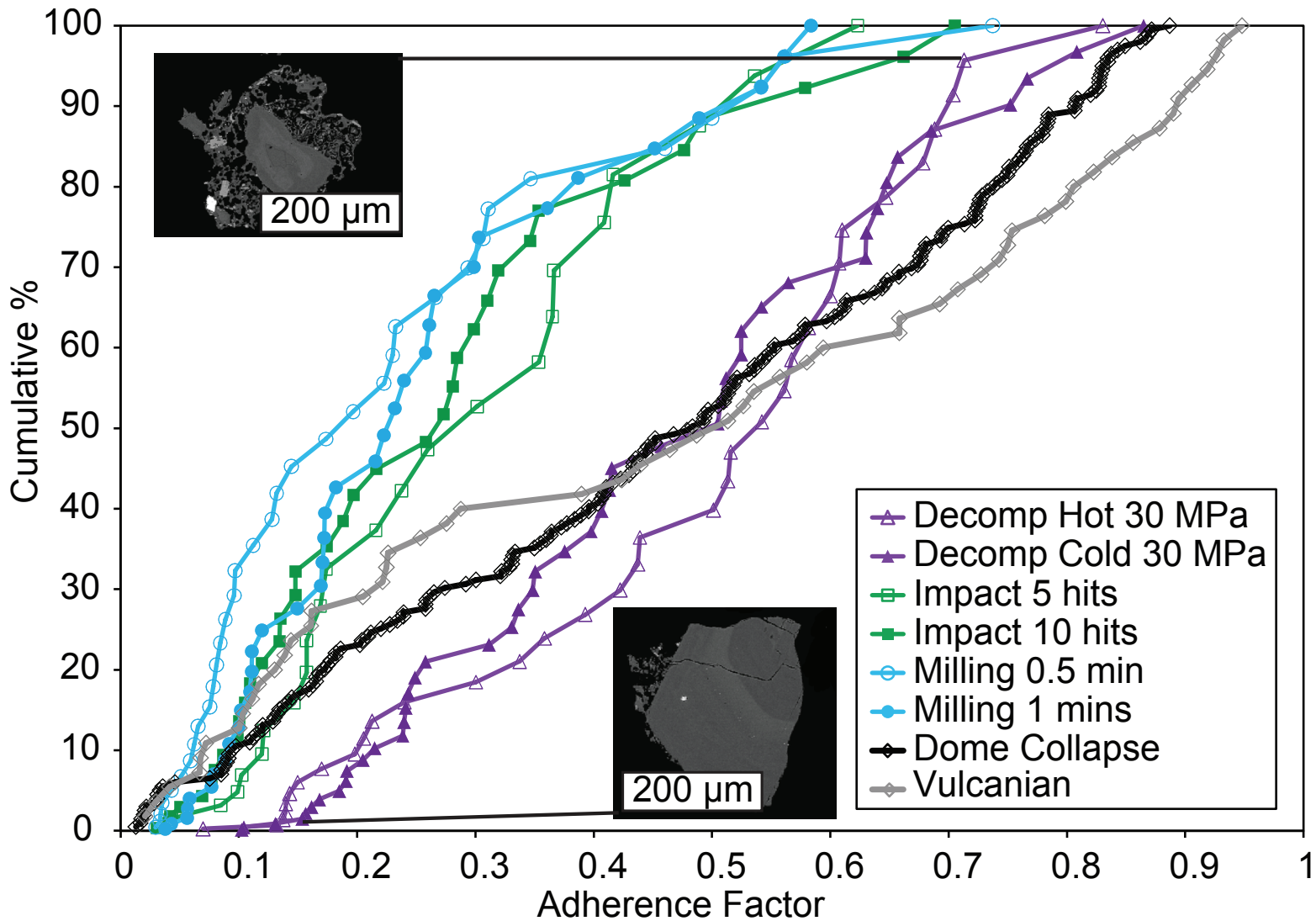
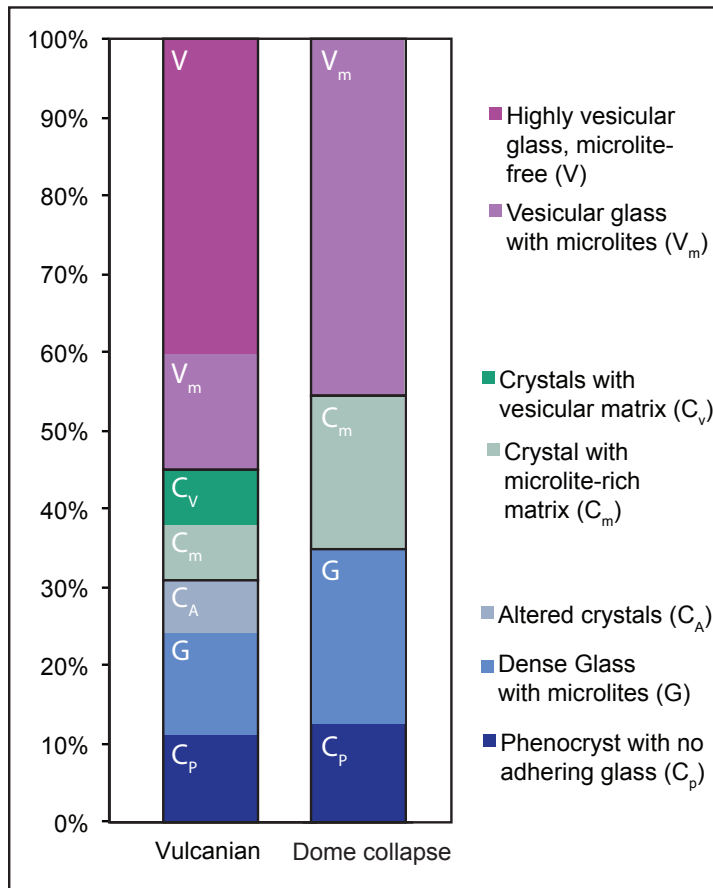


Figure 9: Jones et al. (2016, JGVR)  
 Size: Single column



**Figure 10:** Jones et al. (2016, JVGR)  
Size: Single Column

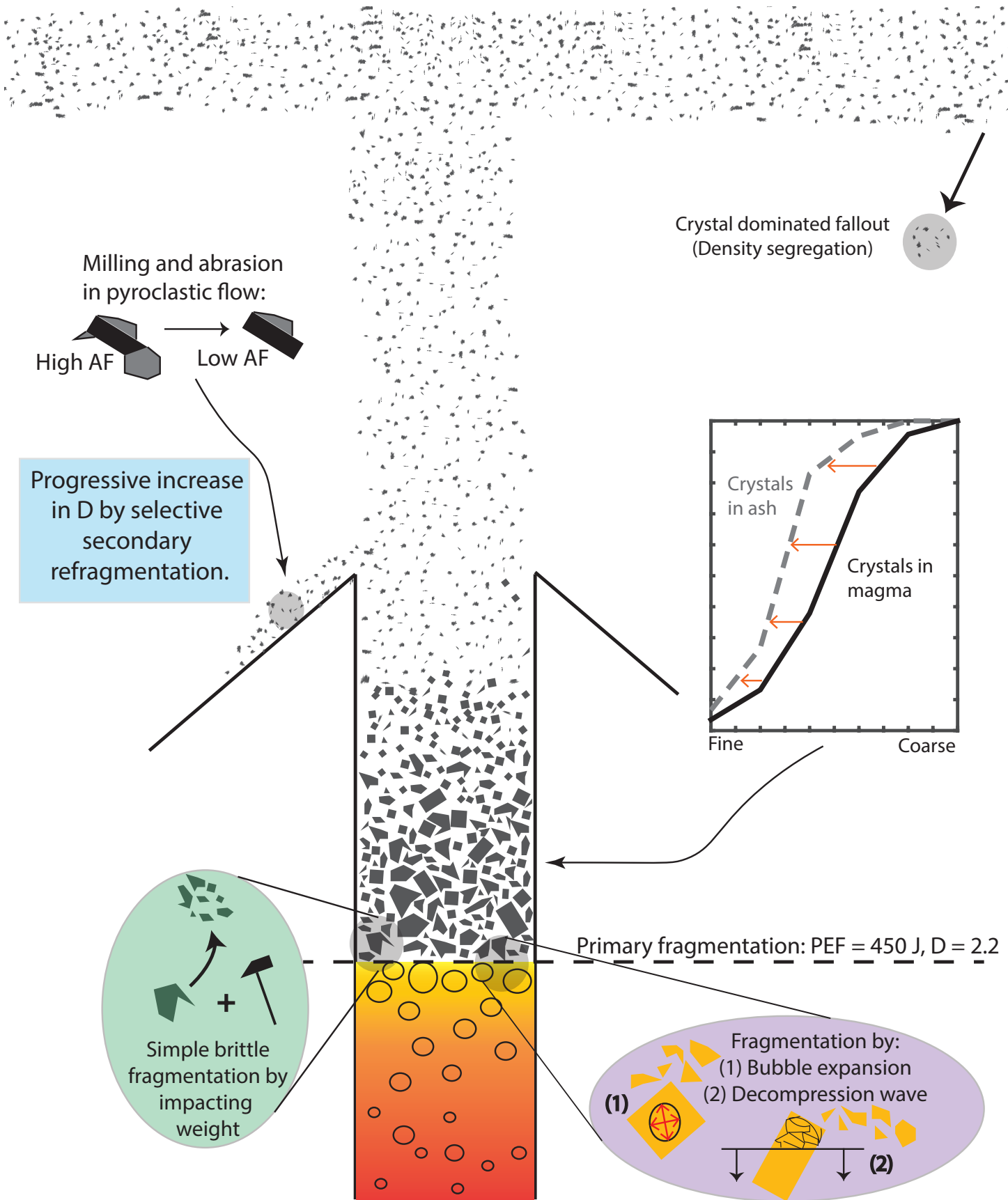


Figure 11: Jones et al (2016, JVGR)  
Size: Single column

**Supplementary Material (Fig s1)**

[Click here to download Electronic Supplementary Material \(online publication only\): Figure\\_S1.pdf](#)



**Supplementary Material (Fig s2)**

**[Click here to download Electronic Supplementary Material \(online publication only\): Figure\\_S2.pdf](#)**